Unsteady flow about a sphere at low to moderate Reynolds number. Part 1. Oscillatory motion

By EUGENE J. CHANG† AND MARTIN R. MAXEY

Center for Fluid Mechanics, Turbulence and Computation, Brown University, Box 1966, Providence, RI 02912, USA

A direct numerical simulation, based on spectral methods, has been used to compute the time-dependent, axisymmetric viscous flow past a rigid sphere. An investigation has been made for oscillatory flow about a zero mean for different Reynolds numbers and frequencies. The simulation has been verified for steady flow conditions, and for unsteady flow there is excellent agreement with Stokes flow theory at very low Reynolds numbers. At moderate Reynolds numbers, around 20, there is good general agreement with available experimental data for oscillatory motion. Under steady flow conditions no separation occurs at Reynolds number below 20; however in an oscillatory flow a separation bubble forms on the decelerating portion of each cycle at Reynolds numbers well below this. As the flow accelerates again the bubble detaches and decays, while the formation of a new bubble is inhibited till the flow again decelerates. Steady streaming, observed for high frequencies, is also observed at low frequencies due to the flow separation. The contribution of the pressure to the resultant force on the sphere includes a component that is well described by the usual added-mass term even when there is separation. In a companion paper the flow characteristics for constant acceleration or deceleration are reported.

1. Introduction

An essential part of determining particle transport in laminar or turbulent flows is the specification of the resultant fluid forces which act on a particle and the subsequent particle motion in response to these forces. Basset (1888) gave an analytical solution for the motion of a small spherical particle settling from rest under gravity in still fluid, based on the assumption of low particle Reynolds number. Within this range of unsteady Stokes flow Basset demonstrated the effects of added-mass and viscous drag forces, both the usual Stokes drag contribution and a history term representing the effects of the finite timescale on which vorticity diffuses through the fluid away from the rigid spherical particle. Since then several adaptations and extensions to Basset's result have been made and a general version given by Maxey & Riley (1983) incorporates the possible effects of an ambient unsteady or non-uniform flow, and a general motion of the particle. The underlying assumptions though remain that the particle Reynolds number is very low, so that locally the disturbance flow due to the presence of the particle is an unsteady Stokes flow, and that the particle size is small compared to the scale on which the ambient flow may vary.

What happens at finite Reynolds numbers or finite particle size is still not clear.

† Present Address: Naval Research Laboratory, Code 6410, Washington, DC 20375, USA

For example a water droplet 300 μm in diameter settling in air will typically remain spherical under the influence of surface tension and behave essentially as a rigid sphere owing to the large difference in the viscosities of air and water. The corresponding Reynolds number is about 20, based on the diameter and terminal fall speed. Similarly an air bubble, of the same size, in water will be spherical owing to surface tension. Further the presence of surface contaminants, found in all but the cleanest water, will for a bubble of this size make it respond approximately as a rigid sphere. Under these conditions the bubble Reynolds number as it rises under buoyancy is about 10. These issues are discussed further in the excellent review of Clift, Grace & Weber (1978). The effect of added-mass is well defined where the flow around the body is inviscid and irrotational (Batchelor 1967), but whether the same is true at finite Reynolds numbers or in flows containing vorticity is not certain. A significant contribution in this direction was made by Auton, Hunt & Prudhomme (1988). They considered the motion of a spherical bubble in an inviscid flow which contained weak vorticity, with a non-uniform ambient flow. They were able to demonstrate the appropriateness of the added mass concept in this context and the correct form it takes for a single spherical particle.

The focus of this paper is to investigate the unsteady flow about a rigid sphere within the particle Reynolds number range $Re \leqslant 50$. The flow far from the sphere is assumed to be of the form

$$U = U(t)e^{(1)}, \qquad (1.1)$$

where the unit vector $e^{(1)}$ is then an axis of symmetry for the flow around the sphere and $U(t)$ allows for various unsteady ambient flow conditions. The flow is further assumed to be axisymmetric with no swirl flow component. We seek to investigate the flow characteristics near the sphere and determine the various fluid forces on the sphere.

Theoretical results for steady, uniform flow past a rigid sphere are given by Proudman & Pearson (1957). They applied matched asymptotic procedures for low Reynolds numbers to determine both the flow field and the fluid drag force as a function of Reynolds number, their results being valid for $Re < 1$. Beyond this range data have come from experimental determination of drag forces or from direct computations of the flow. Standard empirical drag laws for varying Reynolds numbers are summarized by Clift et al. (1978). Computations of steady axisymmetric flow past a sphere have been conducted by Rimon & Cheng (1969), Le Clair, Hamielec & Pruppacher (1970) and more recently by Fornberg (1988), all based on finite-difference schemes. A different computational approach based on an expansion in terms of Legendre functions and spherical harmonics was used by Dennis & Walker (1971), Oliver & Chung (1985), and by Brabston & Keller (1975) in the context of a spherical gas bubble. These simulations give results consistent with the experimental data for the drag forces, and have been used to develop improved formulae. The computations also have demonstrated the formation of a separated flow region, with a bubble of recirculating flow behind the sphere, for Reynolds numbers greater than 20.5. These features agree with the earlier flow visualization experiments of Taneda (1956), who noted that the length of the separation bubble grows linearly with the logarithm of the Reynolds number. Beyond a Reynolds number of between 120 and 130 the wake region behind the sphere becomes unstable and flow is inherently unsteady. Stability characteristics of the wake have been investigated by Kim & Pearlstein (1990), Natarajan & Acrivos (1993), and by Tomboulides, Orszag & Karniadakis (1993).

Bentwich & Miloh (1978) and Sano (1981) have extended the matched asymptotic procedures of Proudman & Pearson (1957) to consider the flow around a sphere which is impulsively set into motion with a specified velocity. Specifically they examine the transient flow development at low Reynolds numbers. Their results exclude added-mass effects since there is no acceleration but indicate how the drag force develops from zero to the final steady flow value. At early times Sano showed that the usual Basset solution applies with appropriate higher-order corrections, but that at longer times there is a faster approach to steady flow conditions. A computational investigation of this transient flow development was carried out by Dennis & Walker (1972) and by Lin & Lee (1973).

Experiments for a sphere in an oscillatory external flow have been conducted for some time in the context of acoustic streaming (Lane 1955), where the amplitude of displacements within the fluid is small compared to the sphere diameter. Experiments for large-amplitude oscillations were conducted by Odar (1964) and further reported by Odar & Hamilton (1964). In these latter experiments the instantaneous force on a sphere was measured as it executed a prescribed sinusoidal oscillation in a fluid that was otherwise at rest. An attempt was made to modify the expressions for added-mass, instantaneous drag force and Basset history term in terms of Reynolds number, but in the absence of further data the results are not conclusive.

More recently Drummond & Lyman (1990) have carried out a preliminary, compu-tational study of oscillatory flow past a sphere, mostly in the range of small-amplitude oscillations. They investigated the effects of the oscillatory flow and the steady acous-tic streaming on mass transfer away from the sphere. In another computational study Mei, Lawrence & Adrian (1991) have investigated the characteristics of small-amplitude oscillations in an otherwise steady mean flow past the sphere. Like Sano (1981) they were interested in the long-range behaviour of the Basset history effect at finite Reynolds numbers. They concluded that this effect would decrease much more rapidly at low frequency than the usual Stokes flow estimate would suggest. Rivero (1991) and Rivero, Magnaudet & Fabre (1991) have also reported recent work on the oscillatory axisymmetric flow past a sphere. Their results will be discussed later in the paper.

In the following sections we describe the analytical and computational procedures used in this investigation. We examine the flow structure in oscillatory flow, com-paring results with the experiments of Odar & Hamilton (1964), and determine the contributions to the fluid from pressure variations and viscous shear stresses. In a companion paper (Part 2, Chang & Maxey 1994) we examine the flow struc-ture as the flow undergoes either a constant acceleration or deceleration in the free stream.

2. Equations of motion

The specific system considered is that of a viscous, incompressible flow past a rigid sphere of radius a which is held fixed in an unbounded fluid. Far from the sphere there is an unsteady but unidirectional flow $U(t)e^{(1)}$ in the free stream. The unit vector $e^{(1)}$ is an axis of symmetry for the flow and we restrict attention to axisymmetric flows without swirl. Position coordinates are given by spherical polar coordinates (r, θ, ϕ) with the origin fixed at the centre of the sphere and the polar axis $(\theta = 0)$ aligned with $e^{(1)}$. This flow configuration is illustrated in figure 1. The flow variables are put into non-dimensional form by scaling all lengths by the sphere radius and scaling all velocities by a reference flow speed U_0, for the free-stream velocity $U(t)$. In
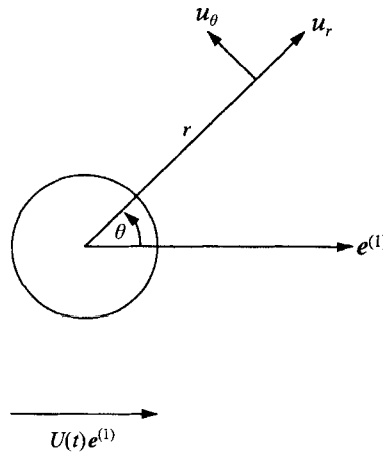
FIGURE 1. Flow configuration.

non-dimensional form the fluid velocity $u(x, t)$ satisfies the equations of motion

$$\frac{\partial u}{\partial t} + u \cdot \nabla u = -\nabla p + \frac{2}{Re}\nabla^2 u,$$ (2.1)

$$\nabla \cdot u = 0,$$ (2.2)

where the pressure p is scaled by ρU_0^2 for a fluid of constant density ρ. The Reynolds number Re is defined in terms of the sphere diameter $2a$ and the kinematic viscosity v as

$$Re = 2aU_0/v.$$ (2.3)

The boundary conditions on the fluid velocity are that

$$u = 0 \quad \text{on} \quad r = 1,$$ (2.4)

$$u = U(t)e^{(1)} \quad \text{as} \quad r \to \infty.$$ (2.5)

These equations are solved by introducing a vector potential for the flow which ensures then that the condition (2.2) of incompressible flow is satisfied exactly. The form of this potential for axisymmetric flow is

$$u = \nabla \times (Ce^{(\phi)}),$$ (2.6)

where $e^{(\phi)}$ is the local unit vector tangential to the ϕ-coordinate. The radial and azimuthal components of velocity are

$$u_r = \frac{1}{r\sin\theta}\frac{\partial}{\partial\theta}(C\sin\theta), \quad u_\theta = -\frac{1}{r}\frac{\partial}{\partial r}(rC).$$ (2.7)

In this formulation the potential function $C(r, \theta, t)$ is related to the more usual Stokes stream function ψ by the relation $\psi = rC\sin\theta$. The pressure is eliminated by forming the equation for the vorticity $\omega = \nabla \times u$, which as the flow is axisymmetric without swirl has only one non-zero component ω_ϕ. The vorticity equation is

$$\frac{\partial\omega_\phi}{\partial t} = (\nabla \times (u \times \omega)) \cdot e^{(\phi)} + \frac{2}{Re}D^2\omega_\phi,$$ (2.8)

where the operator D^2 is defined as

$$D^2 = \nabla^2 - \frac{1}{r^2 \sin^2 \theta}. \tag{2.9}$$

The vorticity and potential function C are related by

$$D^2 C = -\omega_\phi. \tag{2.10}$$

Hereafter the subscript ϕ will be omitted for this vorticity component.

The flow is determined by numerically solving (2.8) for the vorticity and (2.10) for the potential function subject to the boundary conditions (2.4) and (2.5). Spectral methods are used to represent the spatial variation of the flow based on the techniques developed by Orszag (1974) and a time-differencing scheme is used to explicitly advance the flow evolution in time. The spectral representation in the θ-variable is a Fourier series. It is more usual in a spherical geometry to use a series expansion in Legendre polynomials as in the study of Dennis & Walker (1971). The Legendre polynomials give increased resolution at the poles $\theta = 0, \pi$ and are suitable where discontinuities may occur. On the other hand a Fourier representation is more convenient in this context and as shown by Orszag (1974) no singularities arise in practice owing to the vanishing of $\sin \theta$ at the poles. An advantage of the Fourier representation is that fast Fourier transform algorithms may be used to go between physical space and spectral space representations. The procedures based on the Fourier representation may also be extended to fully three-dimensional flows. Another feature is that it gives a uniform spatial resolution on the surface of the sphere which may be more appropriate for unsteady or non-uniform flow conditions where the detailed flow structure is not necessarily confined to some fixed wake region or narrow region at the poles.

Physically all the flow variables u_r, u_θ and ω are continuous and regular at all points in the flow. Along the axis of symmetry, for $\theta = 0$ or π, the azimuthal component of the flow u_θ is zero. The range of the coordinate variables θ and ϕ is normally restricted so that $0 \leqslant \theta \leqslant \pi$ and $0 \leqslant \phi \leqslant 2\pi$ but in principle θ may be varied from $-\pi$ to π with some alternate restriction on ϕ. The point specified by the coordinates (r, θ, ϕ) is unaltered if the transformation

$$\theta \to -\theta, \quad \phi \to \phi + \pi \tag{2.11}$$

is applied. The local radial unit vector $e^{(r)}$ is similarly unaltered while the vector $e^{(\theta)}$ is reversed. Consequently u_r, obtained as $u \cdot e^{(r)}$, is invariant while u_θ changes sign. Under axisymmetric flow conditions there is no dependence of the flow on the value of the ϕ-coordinate so we may conclude that u_r is an even function of θ, u_θ is an odd function and that the vorticity ω is similarly an odd function. The relations (2.7) in turn imply that C is an odd function. Thus the vorticity ω is an odd, periodic function of θ, which is regular and may be represented by a Fourier sine series over the range $0 \leqslant \theta \leqslant \pi$.

The potential function C may also be regarded as a regular, non-singular function at all points in the flow. The definition (2.7) of C in terms of the fluid velocity allows some arbitrariness in that any constant multiple of $(r \sin \theta)^{-1}$ may be added to it without changing the flow. Singularities due to terms of this sort may be ignored. Otherwise the relations (2.7) imply that C is non-singular at the poles. The boundary conditions (2.4) may be reformulated as

$$C = 0, \quad \frac{\partial C}{\partial r} = 0 \quad \text{on} \quad r = 1, \tag{2.12}$$

and at large distances from the sphere

$$\omega = 0, \quad C = \tfrac{1}{2}U(t)r\sin\theta \quad \text{as} \quad r \to \infty. \tag{2.13}$$

2.1. *Evaluation of the drag*

The resultant fluid force on the sphere exerted by the moving fluid is found by integrating the contributions from the stress tensor σ_{ij} over the sphere surface:

$$F_i = \oint \sigma_{ij} n_j \, \mathrm{d}S, \tag{2.14}$$

where $\mathbf{n}$ is the unit outward normal. Since the flow is axisymmetric the force $\mathbf{F}$ acts parallel to the free-stream velocity U and there is no lift force. The component of the force in the direction $\mathbf{e}^{(1)}$ can be expressed in terms of the spherical polar coordinates as

$$F_1 = \oint (\sigma_{rr}\cos\theta - \sigma_{r\theta}\sin\theta)\,\mathrm{d}S. \tag{2.15}$$

The normal component of the stress σ_{rr} is

$$\sigma_{rr} = -p + 2\rho\nu\frac{\partial u_r}{\partial r} \tag{2.16}$$

in dimensional form. The no-slip boundary conditions (2.4) and the condition of incompressible flow (2.2) ensure that $\partial u_r/\partial r$ vanishes on the surface of the sphere so that the only contribution from σ_{rr} is through the pressure. The shear stress $\sigma_{r\theta}$ is

$$\sigma_{r\theta} = 2\rho\nu\left[\frac{r}{2}\frac{\partial}{\partial r}\left(\frac{u_\theta}{r}\right) + \frac{1}{2r}\frac{\partial u_r}{\partial\theta}\right], \tag{2.17}$$

again in dimensional form. Following our previous non-dimensional scaling in terms of the sphere radius, fluid density, and free-stream velocity scale the non-dimensional drag force C_d is defined here as

$$C_d = F_1/\pi\rho a^2 U_0^2. \tag{2.18}$$

The drag force C_d may be split into two separate parts, C_f for the frictional component due to shear stress and C_p for the pressure component with their sum equalling C_d. On the surface of the sphere the no-slip boundary conditions (2.4) lead to the result that the rate-of-strain term in (2.17) is equal to half the local surface vorticity. The frictional component C_f is calculated from (2.15) and (2.17) as

$$C_f = -\frac{4}{Re}\int_0^\pi \omega(r = 1,\theta)\sin^2\theta \, \mathrm{d}\theta, \tag{2.19}$$

in terms of the surface vorticity. The pressure component C_p in non-dimensional form is

$$C_p = -\int_0^\pi p(r = 1,\theta)\sin 2\theta \, \mathrm{d}\theta, \tag{2.20}$$

where the pressure p is non-dimensional, scaled as before by ρU_0^2. A direct evaluation of the pressure can be avoided by considering the momentum equation (2.1) near the surface of the sphere, and in fact the pressure variation over the surface of the sphere can be determined once the vorticity field is known:

$$p(r = 1,\theta) = p(1,\pi) - \frac{2}{Re}\int_\theta^\pi \left.\frac{\partial}{\partial r}(r\omega)\right|_{r=1} \mathrm{d}\theta'. \tag{2.21}$$

In order to compare our results with those of other authors we define a non-dimensional pressure coefficient

$$k(\theta) = \tfrac{1}{2}(p(r = 1, \theta) - p_\infty), \tag{2.22}$$

where p_∞ is the pressure at infinity. The coefficient is equivalent to a scaling of pressure by $\rho U_0^2/2$. The pressure at the stagnation point, $\theta = \pi$, can be evaluated from the radial momentum equation as

$$k(\pi) = \tfrac{1}{2}(p(1, \pi) - p_\infty) = 1 + \frac{8}{Re} \int_1^\infty \frac{1}{r} \frac{\partial \omega}{\partial \theta}\bigg|_{\theta=\pi} dr. \tag{2.23}$$

3. Numerical method

A pseudospectral or collocation method based on the technique developed by Marcus & Tuckerman (1987) is used to advance the equations of motion in time. Functions are presented both in spectral space as a finite series of basis functions and by values at collocation grid points in physical space. Derivatives are obtained from the spectral representation while products are evaluated in physical space. The vorticity ω and the potential C are expanded as a Chebyshev polynomial series in the radial direction and as a sine series in the azimuthal direction. A function $f(r, \theta)$ written in these terms takes the form

$$f(z, \theta) = \sum_{m=0}^{M} \sum_{n=1}^{N} f_{mn} T_m(z) \sin(n\theta), \tag{3.1}$$

where T_m is the Chebyshev polynomial of degree m. In physical space $f(z, \theta)$ is represented at the collocation point

$$\theta_n = \pi n/(N+1) \quad \text{for } n = 1, \dots, N, \tag{3.2}$$

$$z_m = \cos^{-1}(2\pi m/M) \quad \text{for } m = 0, 1 \dots, M. \tag{3.3}$$

An algebraic map

$$r = 1 + L\frac{1+z}{b-z}, \quad |z| \leqslant 1, \tag{3.4}$$

where

$$b = 1 + \frac{2L}{r_\infty - 1} \tag{3.5}$$

and L is a scaling parameter, is used to map the radial interval $1 \leqslant r \leqslant r_\infty$ to the interval $-1 \leqslant z \leqslant 1$. This form of algebraic map was found to give reliable accuracy under a wide range of flow conditions and maintained the spectral accuracy of the scheme. A finite, but large outer radius r_∞ was chosen to avoid regularity problems in the radial differentiation. An example of this map for $M = 64$, with $r_\infty = 50$ and $L = 2$ is shown in figure 2, where r is plotted both as a function of z and of index m for the collocation point (3.3).

The potential C is written as the sum

$$C = \bar{C} + c, \tag{3.6}$$

with the potential $\bar{C}$ corresponding to the prescribed flow in the freestream, typically

$$\bar{C} = \tfrac{1}{2}U(t)r \sin\theta \tag{3.7}$$

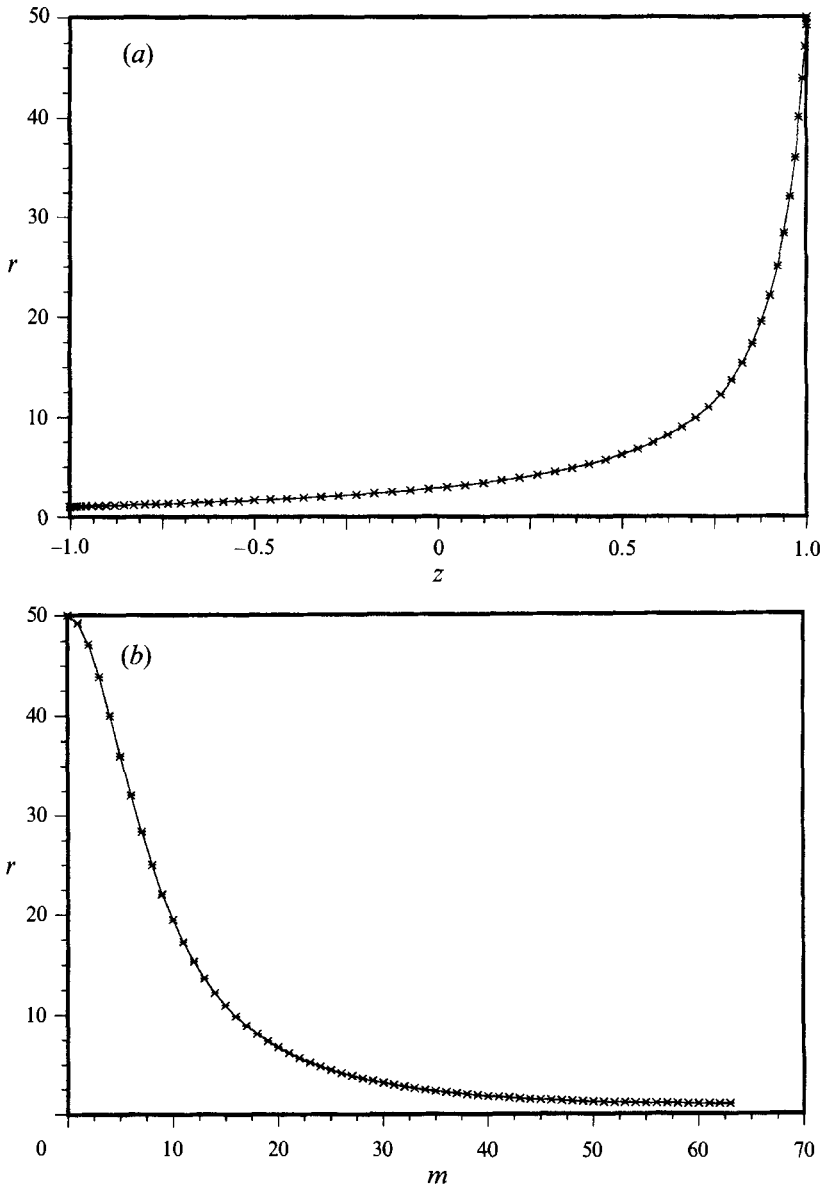as in (2.13). The potential c is then due to the disturbance produced by the presence

FIGURE 2. The map $r = 1 + L(1 + z)/(b - z)$ which maps $|z| \leqslant 1$ to $1 \leqslant r \leqslant r_\infty$, where $b = 1 + (2L)/(r_\infty - 1)$ and $L = $ stretch parameter for $r_\infty = 50$ and $L = 2$, (*a*) as a function of z, and (*b*) as function of grid point index m.

of the sphere. The boundary conditions for the numerical scheme corresponding to (2.12) and (2.13) are

$$c = -\bar{C}, \quad \frac{\partial c}{\partial r} = -\frac{\partial \bar{C}}{\partial r} \quad \text{at } r = 1, \tag{3.8}$$

$$c = 0, \quad \omega = 0 \quad \text{at } r = r_\infty. \tag{3.9}$$

Thus at the outer radius a condition of zero vorticity is maintained, with the radial inflow–outflow matched to the free-stream conditions.

The sine series expansions (3.1) for ω and c match exactly the periodicity conditions

and symmetry conditions in θ discussed previously. The series may be regarded as a Galerkin expansion (Marcus & Tuckerman 1987), or the truncation to N terms of some infinite Fourier expansion (Orszag 1974). To obtain the potential function c from the vorticity ω at any time level requires the solution of the elliptic equation (2.10). Following Marcus & Tuckerman (1987) we define the separable derivative operators D_r^2 and D_θ^2 through

$$r^2 D^2 = D_r^2 + \frac{1}{\sin^2\theta} D_\theta^2, \tag{3.10}$$

with

$$D_r^2 = \frac{\partial}{\partial r}\left(r^2\frac{\partial}{\partial r}\right), \tag{3.11}$$

$$D_\theta^2 = \sin\theta\frac{\partial}{\partial\theta}\left(\sin\theta\frac{\partial}{\partial\theta}\right) - 1. \tag{3.12}$$

In spectral θ-space the effect of the operator D_θ^2 at any fixed radial location (physical r-space) can be written as a matrix *ptptpt***S** which operates on a vector of the N sine series coefficients. For the series

$$f(\theta) = \sum_{j=1}^{N} f_j \sin j\theta, \tag{3.13}$$

the corresponding sine series coefficients of $D_\theta^2 f$ are the components of the vector $S_{ij} f_j$ where

$$S_{ij} = \begin{cases} 1/4(i-2)(i-1) & \text{for} \quad i = j+2 \\ -1 - 1/2i^2 & \text{for} \quad i = j \\ 1/4(i+2)(i+1) & \text{for} \quad i = j-2 \\ 0 & \text{otherwise.} \end{cases} \tag{3.14}$$

This matrix is $N \times N$ if the representation for $D_\theta^2 f$ is truncated to N Fourier terms. Similarly the operation of multiplying a function $f(\theta)$ by $\sin^2\theta$ can be written as a matrix **Q**, which has a similar structure. Again the matrix **Q** is $N \times N$ if the representation of $\sin^2\theta f(\theta)$ is truncated to N terms. There is an ambiguity though about possible terms in $\sin(N+1)\theta$ or $\sin(N+2)\theta$, especially if the series (3.13) itself is a truncated series. The combined operator $(1/\sin^2\theta)D_\theta^2$ is equivalent to $\mathbf{Q}^{-1}\mathbf{S}$ and can be written as an $N \times N$ matrix **A** where the only non-zero elements are

$$A_{ij} = \begin{cases} a1(i) = -i(i+1) & \text{for} \quad i = j, \\ a2(i) = -2i & \text{for} \quad i < j, \; i+j \text{ even.} \end{cases} \tag{3.15}$$

This is the result given by Marcus & Tuckerman (1987). As noted by Orszag (1974) the ambiguity of the higher-order Fourier terms is resolved by requiring that the representation of $(1/\sin^2\theta)D_\theta^2 f(\theta)$ be regular at the poles.

3.1. *Time integration*

Time integration of the vorticity equation (2.8) is accomplished through use of an explicit second-order Adams–Bashforth scheme for the nonlinear terms and an implicit second-order Crank–Nicolson scheme for the viscous and linear terms. The calculations are made in physical r-space and spectral θ-space. If we denote by $\hat{\omega}(r,t)$

the vector of N sine series coefficients for the vorticity, then the discretized forms of equations (2.8) and (2.10) are

$$\left[D_r^2 - r^2 \frac{Re}{\Delta t} + \mathbf{A} \right] \hat{\omega}(r, t + \Delta t) = \hat{\mathbf{R}}(t), \tag{3.16}$$

$$\left[D_r^2 + \mathbf{A} \right] \hat{c}(r, t + \Delta t) = -r^2 \hat{\omega}(r, t + \Delta t), \tag{3.17}$$

where

$$\hat{\mathbf{R}}(t) = - \left[D_r^2 + r^2 \frac{Re}{\Delta t} + \mathbf{A} \right] \hat{\omega}(r, t) - \frac{Re}{2} r^2 [3\hat{G}(t) - \hat{G}(t - \Delta t)], \tag{3.18}$$

$$G = (\nabla \times (\boldsymbol{u} \times \boldsymbol{\omega})) \cdot e^{(\varphi)}. \tag{3.19}$$

The radial derivatives are evaluated by collocation methods and expressed as matrix operations on the vector of function values at the grid points in physical r-space. For the representation (3.1) with $(M + 1)$ collocation points we introduce the $(M + 1) \times (M + 1)$ matrix operation $ptptpt\mathbf{D}^{(1)}(n)$,

$$\mathbf{D}^{(1)}(n) = \mathbf{D}_r^2 + \left[a1(n) - \frac{Re}{\Delta t} r^2 \right] \mathbf{I} \tag{3.20}$$

where $\mathbf{D}_r^2$ is the matrix corresponding to D_r^2 and $\mathbf{I}$ is the identity matrix. The operator $\left[D_r^2 - r^2(Re/\Delta t) + \mathbf{A} \right]$ acting on $\hat{\omega}(r, t + \Delta t)$ in (3.16) may now be written in block matrix form as

$$\begin{bmatrix} \mathbf{D}^{(1)}(1) & 0 & a2(1)\mathbf{I} & 0 & a2(1)\mathbf{I} & 0 & \cdots \\ & \mathbf{D}^{(1)}(2) & 0 & a2(2)\mathbf{I} & 0 & a2(2)\mathbf{I} & \cdots \\ & & \mathbf{D}^{(1)}(3) & 0 & a2(2)\mathbf{I} & 0 & \cdots \\ & & & \mathbf{D}^{(1)}(4) & 0 & a2(4)\mathbf{I} & \cdots \\ & & & & \cdot & \cdot & \cdot \\ & & & & & \cdot & \cdot \\ & & & & & & \cdot \end{bmatrix}. \tag{3.21}$$

This matrix acts on the vector of length $(M + 1) \times N$ of the vorticity coefficients $(\hat{\omega}_1(r_0), \hat{\omega}_1(r_1), \ldots, \hat{\omega}_1(r_m), \hat{\omega}_2(r_0), \ldots, \hat{\omega}_N(r_m))$. Equation (3.16) is an upper triangular, block matrix problem in physical r-space and spectral θ-space which can be solved by back substitution with the Dirichlet boundary conditions discussed below. The equation (3.17) is treated in the same manner and leads to an upper triangular, block matrix problem with each diagonal term on row n replaced by $\mathbf{D}_r^2 + a1(n)\mathbf{I}$.

3.2. Green's function method

To enforce the radial boundary conditions a Green's function method has been developed which gives the correct boundary conditions (3.8)–(3.9) and allows the
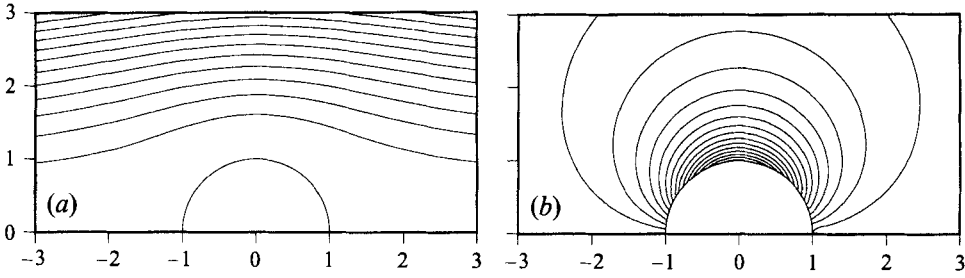
FIGURE 3. (*a*) Streamlines for $Re = 0.1$; $\Delta\psi = 0.25$. (*b*) Lines of constant vorticity for $Re = 0.1$; $\Delta\omega = 0.1$.

surface vorticity to develop naturally. The procedure follows similar approaches by Marcus & Tuckerman (1987) and Kim, Moin & Moser (1987). The discretized equations (3.16) and (3.17) for the time stepping of the vorticity and potential function may be written as the coupled system

$$\left.\begin{array}{l} E^2\omega(r,\theta,t+\Delta t) = R(r,\theta,t), \\ H^2c(r,\theta,t+\Delta t) = -r^2\omega(r,\theta,t+\Delta t), \end{array}\right\} \tag{3.22}$$

where E^2 and H^2 are the collocation, derivative operators and R is the known, time-dependent, inhomogeneous term given by (3.18). This system is linear in the new variables at time $(t + \Delta t)$ and a solution may be constructed by superposing general and particular solutions which satisfy the homogeneous and inhomogeneous equations respectively. The homogeneous equations, with R equal to zero, are solved first in a preprocessing stage to yield Green's functions $\tilde{\omega}_j$ and $\tilde{c}_j$ that satisfy the time-independent boundary conditions that on the sphere $\tilde{c}_j$ is zero and

$$\tilde{\omega}_j(r = 1,\theta) = \begin{cases} 1 & \text{if} \quad \theta = j\pi/(N+1) \\ 0 & \text{otherwise} \end{cases} \tag{3.23}$$

while $\tilde{\omega}_j$, $\tilde{c}_j$ both vanish at $r = r_\infty$. These functions are saved and combined later in the computation to ensure that the full solution satisfies (3.8) and (3.9). The particular solutions satisfy (3.22) with the corresponding vorticity vanishing at both $r = 1$ and $r = r_\infty$, while the potential function $c_p = -\bar{C}$ on the sphere and is zero at $r = r_\infty$

Further details, together with tests of the numerical scheme are given by Chang (1992).

4. Steady flows

To verify the numerical methods and to provide a comparison for the unsteady flows discussed later, simulations for steady, unidirectional flow were carried out for $Re \leqslant 40$. For these the flow is initially at rest and then a uniform, constant external flow $U(t) \equiv 1$ is introduced in the direction of $\theta = 0$, and the simulation continued till the solution has converged to a steady state. A time step of $\Delta t = 0.005$ is used in all of these calculations, with spatial discretizations of 48×48, 64×64, or 96×96 grid points. The Chebyshev Gauss–Lobatto collocation points, in conjunction with the algebraic map (3.4) yield a clustering of points near the sphere surface. The stretch parameter L is used to control this clustering. Typically for $Re \leqslant 1$ a value of $L=8$ and an outer radius of 250 is used with a 48×48 grid. For higher Reynolds

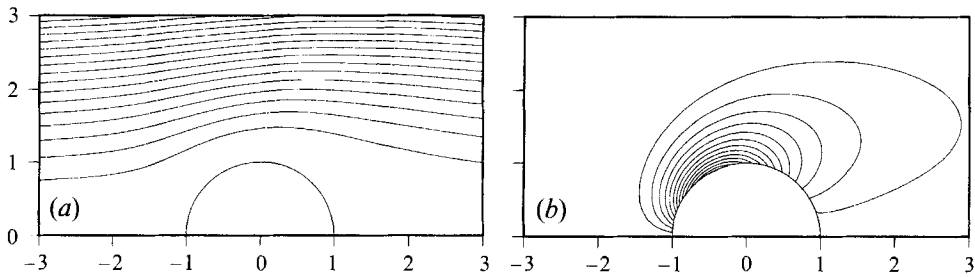FIGURE 4. (a) Streamlines for $Re = 10$; $\Delta\psi = 0.25$. (b) Lines of constant vorticity for $Re = 10$; $\Delta\omega = 0.25$.
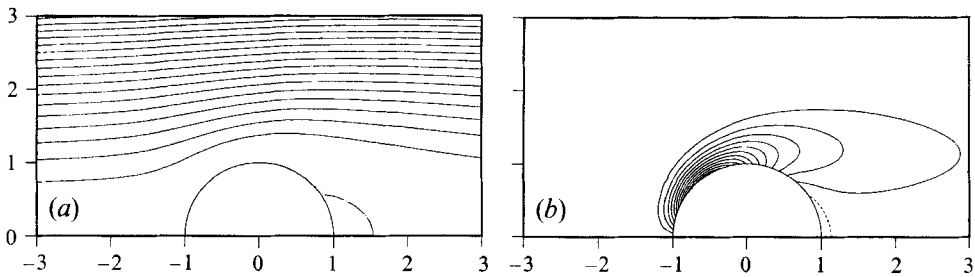

FIGURE 5. (a)Streamlines for $Re = 40$; $\Delta\psi = 0.25$. (b) Lines of constant vorticity for $Re = 40$; $\Delta\omega = 0.5$.

numbers a value of $L=2$ and outer radius of 50 is used with either a 64×64 grid for $Re \leqslant 20$ or a 96×96 grid at larger Reynolds numbers. At low Reynolds numbers the vorticity diffuses over a large region compared to the sphere radius owing to viscous action, while at higher Reynolds numbers the vorticity is convected downstream with a more complex structure, which requires increased resolution.

At low Reynolds numbers the flow is reasonably well described by a Stokes flow, and the vorticity diffuses evenly over a large distance. Figure 3 shows the vorticity and streamlines in the vicinity of the sphere at a Reynolds number of 0.1. A very slight asymmetry about $\theta = \pi/2$ is observable. At higher Reynolds numbers, corresponding diagrams for $Re = 10$ and $Re = 40$ are shown in figures 4 and 5. It is evident that there is a distortion of the vorticity field by advection in the flow and at $Re = 40$ a region of separated flow is clearly visible, with a small localized region of positive vorticity in the near wake of the sphere. The onset of a separation region is indicated when $\partial\omega/\partial\theta$ is zero at the rear stagnation point of the sphere. An estimate of $Re = 20.7$ is given by the current simulations as the Reynolds number for the onset of separation. This is in good agreement with the value of $Re = 20.5$ given by Dennis & Walker (1971) and the value of $Re = 20$ given by both Le Clair et al. (1970) and Lin & Lee (1973). Others have found separation to first occur at different Re, for example Rimon & Cheng (1969) found separation as low as $Re = 10$. The experiments by Taneda (1956) showed separation occurred somewhere between $Re = 22$ and 25 with an estimated onset value of $Re = 24$.

Table 1 lists for the larger Reynolds number simulations the angle θ at which separation was found to occur and the length of the separation bubble as measured downstream from the rear stagnation point. Taneda's data suggest that the length of the separation bubble varies linearly with the logarithm of the Reynolds number. Our

Re	$k(\pi)$	C_f	C_p	C_d				θ_s	l/d
				Present	Goldstein	Proudman & Pearson	Chester & Breach		
0.1	62.3	81.8	40.8	122.6	122.2	122.1	122.1	-	-
0.2	32.1	41.5	20.7	62.2	62.2	61.9	62.0	-	-
0.3	22.0	28.1	14.0	42.1	42.2	41.9	41.95	-	-
0.4	16.9	21.3	10.7	32.0	32.2	31.8	31.9	-	-
0.5	13.9	17.3	8.63	25.9	26.2	25.8	25.9	-	-
0.6	11.9	14.6	7.28	21.9	22.2	21.8	21.9	-	-
0.7	10.4	12.6	6.32	18.9	19.3	18.9	19.0	-	-
0.8	9.29	11.2	5.60	16.8	17.1	16.8	16.9	-	-
0.9	8.43	10.0	5.03	15.1	15.5	15.1	15.3	-	-
1.0	7.74	9.12	4.57	13.7	14.1	13.8	14.0	-	-
					Rimon & Cheng	Le Clair *et al.*	Dennis & Walker		
0.1	62.3	81.8	40.8	122.6	-	122.04	122.1	-	-
1.0	7.74	9.12	4.57	13.7	-	13.66	13.72	-	-
5.0	2.61	2.41	1.26	3.67	-	3.56	3.61	-	-
10.0	1.87	1.43	0.784	2.21	2.21	2.14	2.21	-	-
15.0	1.60	1.07	0.612	1.68	-	-	-	-	-
20.0	1.46	0.863	0.538	1.40	-	1.36	1.40	-	-
25.0	1.38	0.744	0.472	1.22	-	-	-	0.337	0.065
30.0	1.32	0.658	0.427	1.09	-	1.06	-	0.468	0.136
35.0	1.28	0.593	0.394	0.987	-	-	-	0.553	0.204
40.0	1.25	0.542	0.374	0.916	0.930	0.930	0.904	0.614	0.267

TABLE 1. Computed stagnation-point pressure coefficients, computed drag coefficients, separation angle θ_s, and wake length l/d where l is the distance downsteam from the rear of the sphere to the end of the recirculation region and d is the sphere diameter

data, although restricted to $Re \leqslant 40$, are consistent with such a result. It should also be remarked that over this limited range a simple linear relationship with Reynolds number is also a good approximation. Table 1 also lists the computed drag force C_d, based on non-dimensional units (2.18), and these are compared with the results of previous studies including those of Goldstein (1929) and Chester & Breach (1969). The agreement is generally good, and for $Re \leqslant 1$ the results compare well with the estimates of Proudman & Pearson (1957). Indeed the agreement was found to be better here than with various higher order asymptotic results.

The calculations of the drag coefficients depend entirely on the surface pressure distribution and the surface vorticity, giving the contributions C_f (2.19) from the shear stress and C_p (2.20) from the pressure. Figures 6 and 7 show the variation in these distributions on the surface of the sphere. The development of flow separation is visible from the surface vorticity at higher Reynolds numbers, where a local region of positive vorticity develops near the rear stagnation point, $\theta = 0$. Correspondingly the surface pressure shows a more significant adverse pressure gradient as the rear stagnation point is approached, at higher Re. The non-dimensional stagnation-point pressure coefficient $k(\pi)$, defined by (2.23), is listed in table 1. The values of this pressure coefficient at the forward stagnation point are in excellent agreement with the results of Dennis & Walker (1971). The values approach the inviscid value of $k(\pi) = 1$ as the Reynolds number increases, and for $Re \geqslant 20$ are generally in agreement with the estimates of Homann (1936) based on boundary-layer theory.
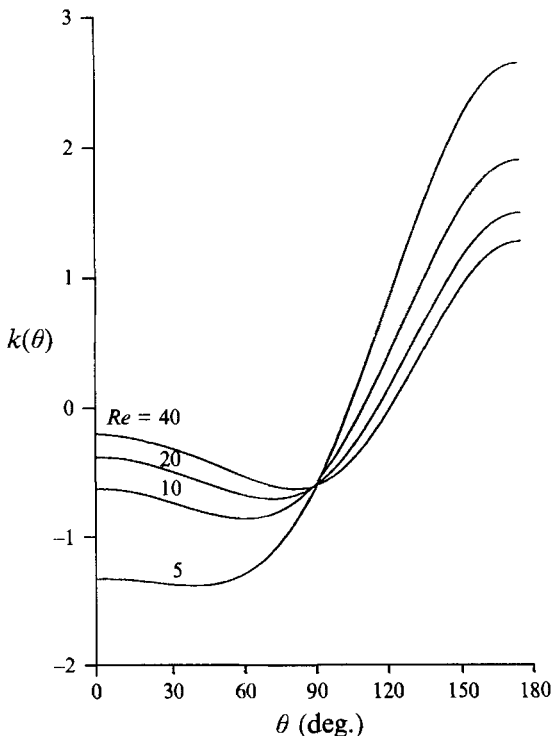
FIGURE 6. Surface pressure distribution for steady flow at $Re = 5, 10, 20$ and 40; $\theta = 180$ corresponds to the upstream stagnation point.

5. Oscillatory flow

For the oscillatory flow case, the external flow field is prescribed as a purely sinusoidal motion with zero mean. The frequency of the oscillation is σ and the amplitude of the fluid displacement in the far field A_0. The velocity of the fluid far from the sphere is parallel to the axis of symmetry and is given by $U = U(t)e^{(1)}$ with

$$U(t) = -A_0\sigma \sin \sigma t. \tag{5.1}$$

The corresponding potential function $\overline{C}$ for the free-stream conditions is given by (3.7) as

$$\overline{C}(t) = -\frac{A_0\sigma}{2}r \sin \theta \sin \sigma t. \tag{5.2}$$

The reference velocity scale of the flow field, U_0, is set equal to $A_0\sigma$, the maximum flow speed in the free stream.

In formulating the vorticity and stream function equations, as in §2, the dimensional radial coordinate r' is scaled by the sphere radius a and the dimensional velocity u' by the reference velocity scale U_0 so that $r = r'/a$ and $u = u'/A_0\sigma$. The Reynolds number (2.3) is defined also through the peak velocity during an oscillation cycle and is given as $Re = 2A_0\sigma a/\nu$. The non-dimensional frequency S_t, or Strouhal number, is then a measure of the relative amplitude of the oscillations,

$$S_t \equiv \sigma a/U_0 = a/A_0. \tag{5.3}$$

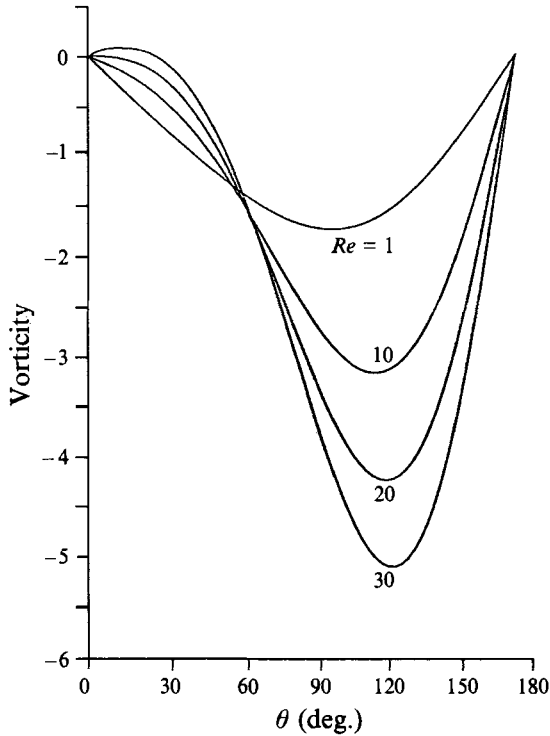We have restricted this study to $Re < 20$ and $S_t < 10$. It is convenient to now introduce

FIGURE 7. Surface vorticity distribution for steady flow at $Re = 5, 10, 20$ and 40 with the azimuthal angle θ given in degrees.

two parameters later used for analysis. The first is the acceleration parameter Ac, which is the ratio of the scale $U_0^2/(2a)$ for the convective acceleration in the flow to the scale σU_0 for the temporal acceleration. Ac is proportional to the Keulegan–Carpenter number K (Keulegan & Carpenter 1958), and inversely proportional to the Strouhal number:

$$Ac = K/2\pi = A_0/2a = 1/2S_t. \tag{5.4}$$

The second parameter of interest, denoted M^2, is the square of the ratio of the sphere radius a, to the Stokes lengthscale $(v/\sigma)^{1/2}$ for viscous diffusion:

$$M^2 = \frac{a^2\sigma}{v} = \tfrac{1}{2}ReS_t. \tag{5.5}$$

At low frequencies and for large-amplitude oscillations the convective acceleration term is the dominant inertial effect. Under these conditions the non-dimensional scheme adopted here of scaling by a and U_0 or σA_0 is physically relevant. The time variable is scaled similarly and the phase angle ϕ of an oscillation cycle is defined by $\sigma t'$ in terms of dimensional variables, or equivalently $S_t t$ with non-dimensional variables. So the non-dimensional forms of the free-stream velocity (5.1) and the potential function (5.2) are

$$U(t) = -\sin\phi, \tag{5.6}$$

$$\overline{C}(t) = -\frac{r}{2}\sin\theta\sin\phi. \tag{5.7}$$

The computations were performed with the vorticity equation as given by (2.8) and the

boundary conditions (3.8) and (3.9). At very high frequencies, with small-amplitude oscillations, S_t is large and the temporal accelerations dominate any convective inertial effects. For the computations in this range a separate formulation was needed with the frequency of the oscillation used to define the timescale. Lengths and velocities were still scaled by the sphere radius a and the maximum flow speed σA_0.

The magnitude of the peak free-stream velocity, $A_0 \sigma$, and the density ρ are used to scale the pressure coefficient:

$$k(\theta) = \frac{p(\theta) - p_\infty}{\frac{1}{2}\rho(A_0\sigma)^2}. \tag{5.8}$$

Of interest is the relative variation of pressure over the surface of the sphere and not specific values. Therefore results are quoted relative to the pressure at $\theta = \pi$ which is assigned a reference value of zero, $k(\pi) = 0$.

The code used to obtain the steady flow results, with appropriate changes to the free-stream and boundary conditions, was used for these simulations. Typically, the time step used was $O(10^{-3})$ and the number of grid points used was 64^2 with stretch parameter $L = 2$ and $r_\infty = 50$. At low frequencies ($S_t \ll 1$) the flow is highly diffusive in nature and vorticity extends throughout much of the flow field. In calculating these flow fields, a 96^2 grid was used with map parameters $L = 4$ and $r_\infty = 150$.

5.1. *Validation*

In order to check the flow simulations, results are first compared with the analytic unsteady Stokes flow solution given by Basset (1888) for a rigid sphere undergoing arbitrary rectilinear acceleration in a still fluid. The velocities and particle diameter are considered to be sufficiently small so that the convective acceleration term in the equations of motion is neglected. The resultant fluid force acting on a sphere which starts from rest and moves with velocity $V(t)$ through otherwise still fluid is

$$-\frac{1}{2}\left(\frac{4}{3}\pi a^3\right)\rho\dot{V}(t) - 6\pi a\mu V(t) - 6\pi a^2\mu \int_0^t \frac{\dot{V}(s)}{[\pi\nu(t-s)]^{1/2}}\,ds, \tag{5.9}$$

where $\dot{V}(t)$ is the acceleration of the sphere. This formula includes the inviscid added-mass effect, a viscous drag force equal to the linear Stokes drag at the same velocity, and and additional viscous drag force from the Basset history term.

For the sinusoidal oscillating flow under consideration, the reference frame is changed to one in which the sphere is fixed and the external flow is given by (5.1) so that $V(t)$ is now replaced by $A_0\sigma \sin\sigma t\, e^{(1)}$. After a long period of time, the lower limit of the integral in (5.9) may be set to $-\infty$ indicating that initial transients to the motion have died out. The force then on a stationary sphere in a viscous fluid oscillating sinusoidally in the free stream with a small-amplitude, high-frequency velocity is given non-dimensionally by

$$-C_{dB} = 2S_t\cos S_t t + \frac{12}{Re}\sin S_t t + \frac{12M}{Re}\cos(S_t t - \pi/4) \tag{5.10}$$

based on the scaling (2.18). A term equal to $\frac{4}{3}S_t\cos(S_t t)$ is included in (5.10) that corresponds to the inertial force from the change of reference frame. Figure 8 shows the difference between the drag given by (5.10) and the drag calculated from a full simulation with $Re = .1$ and $S_t = 10$. These results compare favorably with Basset's result with the maximum relative error less than $O(10^{-3})$. The difference is itself almost sinusoidal and indicates that the difference between the actual computed drag force and the analytical result (5.10) is primarily attributable to a phase shift between
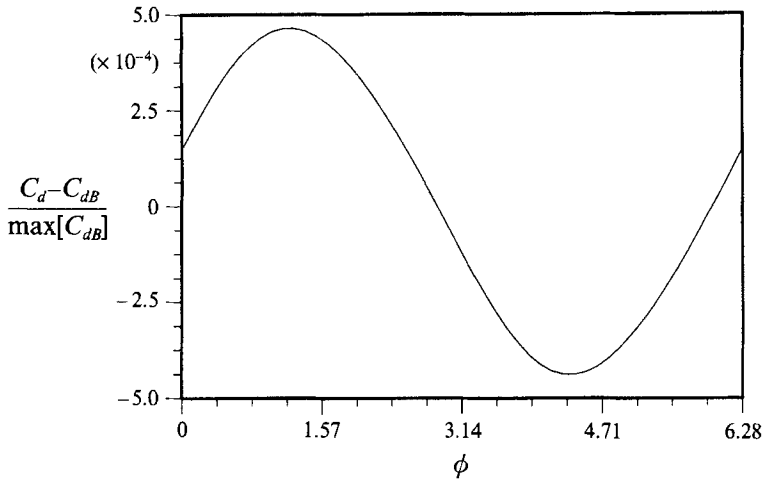
FIGURE 8. $(C_d - C_{dB})/\max[C_{dB}]$ versus ϕ for $Re = 0.1$ and $S_t = 10$; C_{dB} is the drag coefficient corresponding to the Basset solution.

the two. The form of (5.10) implies that the force varies only at the frequency of the flow oscillation, there being no harmonics present. The Fourier time spectrum of the calculated force is shown in figure 9 and indeed shows little harmonic content. The third harmonic, which is the only one observed, is ten orders of magnitude less than the fundamental and is negligible.

To further test our numerical simulation, results are also compared with the experimental data provided by Odar (1964). Results for $Re = 16.7$ and $S_t = 0.625$ are shown in figure 10, which corresponds to run 9 of Odar's experiments. The results compare favourably to Odar's experimental data, with the maximum error occurring just before the force peaks during a cycle. This coincides with an area where the experimental data were erratic and had to be smoothed. In addition, the tank used to contain the fluid in which the sphere was moving had an effective outer radius of 14.4 radii which may have affected the results. However, our simulations for this $Re - S_t$ combination indicate only minor changes in results for different $r_\infty > 15$ with a 0.4% difference in force at maximum free-stream velocity between results obtained at $r_\infty = 15$ and $r_\infty = 150$. At $r = 14.4$ the vorticity field is $O(10^{-5})$ throughout the oscillation cycle, indicating that the outer boundary probably had little effect on Odar's results. Comparisons with other sets of data obtained by Odar yield similar results.

5.2. *Flow characteristics*

Figures 11 and 12 show a sequence of streamline and vorticity contours over half an oscillation cycle for $Re = 16.7$ and $S_t = 0.625$. Figures 13 and 14 show the corresponding relative surface pressure and surface vorticity distributions. The sequence begins just after the free-stream has reversed direction and has started to flow from right to left, towards the direction of $\theta = \pi$. There are distinct inner and outer regions of vorticity of opposite sign which exist throughout the flow cycle. Even at peak free stream velocity the attached vorticity, generated at the surface (which is designated as the inner region), remains confined to an area very close to the sphere. Upon deceleration of the free stream the flow separates and the vorticity starts to detach from the sphere. This detached (now outer) region of vorticity generated during the
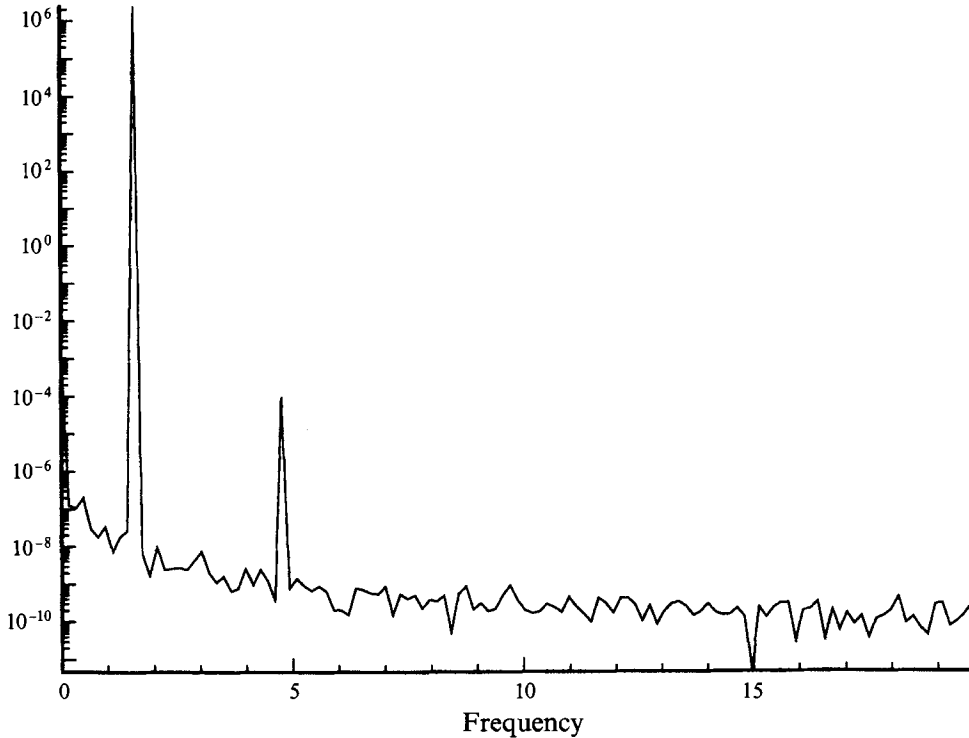
FIGURE 9. Fourier time spectrum for C_d with $Re = 0.1$ and $S_t = 10$;
fundamental frequency is $S_t/2\pi$.

acceleration phase is much weaker than the inner region of vorticity generated during deceleration. As each half-oscillation cycle is completed, a new region of surface-generated vorticity (of opposite sign) detaches creating the layering effect seen in the vorticity contours. Examination of flows at other Reynolds and Strouhal numbers yields similar flow patterns.

Although separation does not occur for $Re < 20$ in steady flows, the development of such a separation region during the deceleration phase of the oscillation is not completely unexpected. Boundary-layer theory predicts that separation can occur in decelerating flows due to the effects of an adverse pressure gradient (cf. Batchelor 1967). Indeed, in this investigation, separation is only found during free-stream deceleration. Table 2 shows the length of the recirculation region at the rear of the sphere, l, and the separation angle measured from the rear of the sphere at $\theta = \pi$ towards the front on the sphere surface in radians, $\Delta\theta_s$, at $\phi = 4\pi/5$. At lower Strouhal numbers (higher-amplitude flows), the separation region is much longer at the rear of the sphere than at higher S_t, with a smaller separation angle. Conversely, at higher Strouhal numbers, the separation region extends a shorter distance downstream at the rear of the sphere but has a larger separation angle. Similarly the downstream length of the region decreases and the separation angle increases with lower Reynolds number.

Also given in table 2 is the phase angle at which separation is first observed, ϕ_s. As the Strouhal number increases, ϕ_s approaches the limiting value $\phi_s = 3\pi/4$. This limiting value is the same as that given by the Basset solution (5.11) for high-frequency,
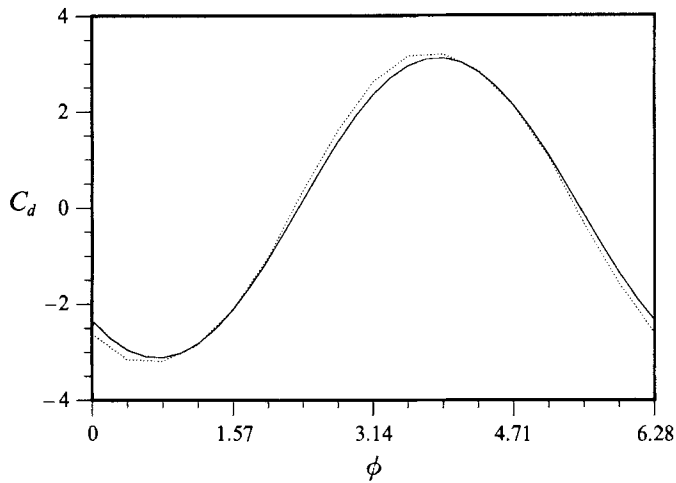
FIGURE 10. Computed and measured experimental drag forces (Odar 1964) over an oscillation cycle for $Re = 16.7$ and $S_t = 0.625$: simulation (———); experiment ($\cdots\cdots$).
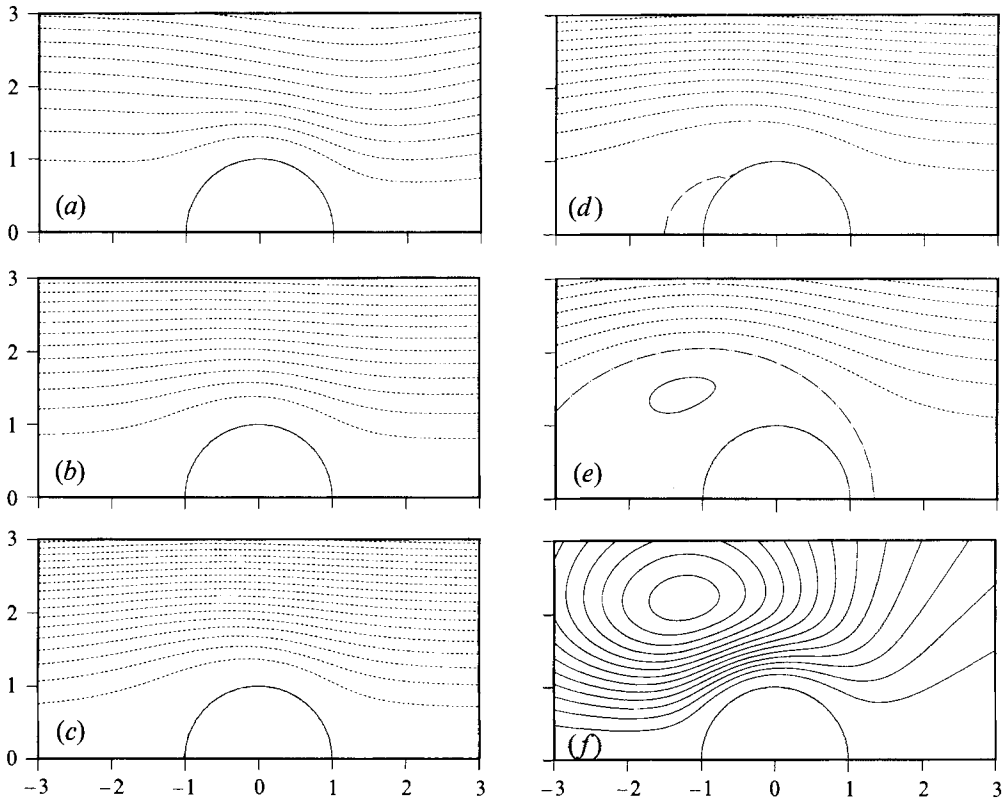

FIGURE 11. Streamline patterns over half an oscillation cycle for $Re = 16.7$ and $S_t = 0.625$ for $U(t) = -\sin(\phi)$; (*a*) $\phi = \pi/16$, $\Delta\psi = 0.1$; (*b*) $\phi = \pi/4$, $\Delta\psi = 0.25$; (*c*) $\phi = \pi/2$, $\Delta\psi = 0.25$; (*d*) $\phi = 3\pi/4$, $\Delta\psi = 0.25$; (*e*) $\phi = 15\pi/16$, $\Delta\psi = 0.1$; (*f*) $\phi = \pi$, $\Delta\psi = 0.025$. $\psi < 0$ (— — —), $\psi = 0$ (— $\cdot$ —), and $\psi > 0$ (———).
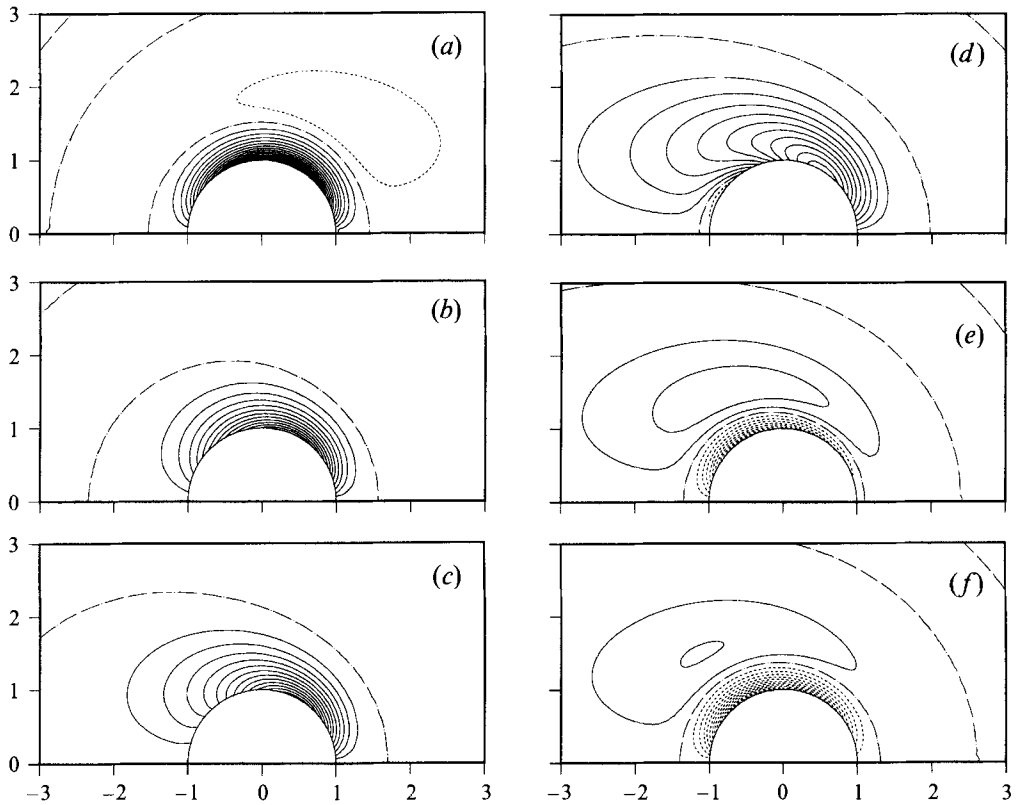
FIGURE 12. Vorticity contours over half an oscillation cycle for $Re = 16.7$ and $S_t = 0.625$; (a) $\phi = \pi/16$, $\Delta\omega = 0.2$; (b) $\phi = \pi/4$, $\Delta\omega = 0.4$; (c) $\phi = \pi/2$, $\Delta\omega = 0.6$; (d) $\phi = 3\pi/4$, $\Delta\omega = 0.2$; (e) $\phi = 15\pi/16$, $\Delta\omega = 0.2$; (f) $\phi = \pi$, $\Delta\omega = 0.2$. $\omega < 0$ (— — —), $\omega = 0$ (— · —·), and $\omega > 0$ (———).

Re	S_t	l	$\Delta\theta_s$	ϕ_s
0.1	0.625	-	-	3.04
1.0	0.625	-	-	2.83
5.0	0.625	0.158	0.558	2.45
10.0	0.625	0.624	1.05	2.35
16.7	0.1	1.83	0.636	1.71
16.7	0.625	0.845	1.22	1.96
16.7	1.0	0.599	1.34	2.08
16.7	2.5	0.269	1.62	2.23
16.7	10.0	0.082	*	2.34
0.01	10.0	-	-	3.01
0.1	10.0	-	-	2.82
1.0	10.0	-	-	2.56
10.0	10.0	0.085	*	2.37
0.1	0.1	-	-	3.10
1.0	0.1	-	-	2.99
10.0	0.1	-	-	2.55

TABLE 2. Length, l, and separation angle in radians, $\Delta\theta_s$, of recirculation region at $\phi = 4\pi/5$; - indicates separation has not yet occurred; ϕ_s is the phase angle at which separation is first observed; * indicates that the bubble completely encompasses the sphere at this phase angle
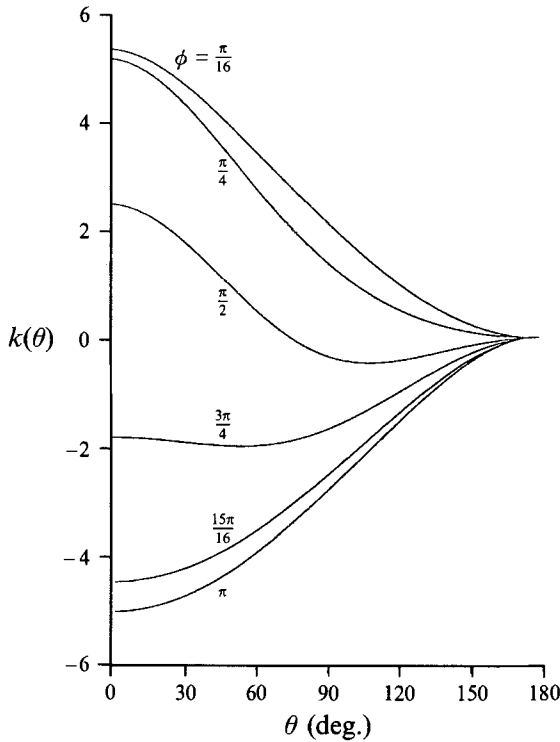
FIGURE 13. Surface pressure, relative to the value at $\theta = 180°$ over half an oscillation cycle for $Re = 16.7$ and $S_t = 0.625$ at $\phi = \pi/16$, $\pi/4$, $\pi/2$, $3\pi/4$, $15\pi/16$, and π.

unsteady Stokes flow conditions for which the surface vorticity is

$$\omega(r = 1, \theta) = \tfrac{3}{2} \sin \theta \{ M \cos(\phi - \pi/4) + \sin \phi \}, \tag{5.11}$$

and the variation in surface pressure is

$$p(r = 1, \theta) = \cos \theta \left\{ \frac{3}{Re} \sin \phi + \frac{3M}{Re} \cos(\phi - \pi/4) + \frac{3}{2} S_t \cos \phi \right\}. \tag{5.12}$$

This limiting behaviour may be expected since for any fixed Reynolds number the increase in the value of S_t is associated with smaller-amplitude oscillations (5.3) and the vorticity is eventually confined to the relatively thin Stokes layer on the surface of the sphere. The large value of M (5.5) implies that the nonlinear convective acceleration terms in the equation of motion are negligible, at least as a first approximation. Thus, even if the value of Re is large the drag force is given by Basset's result (5.8). At low fixed Reynolds numbers, the phase angle ϕ_s for the onset of separation increases towards π as the Strouhal number is reduced. This represents more of a quasi-steady response since the free-stream velocity reverses at $\phi = \pi$. The angle of separation is associated with the point at which the surface shear stress, or equivalently (2.19) the surface vorticity, changes sign. Under conditions of Stokes flow the Basset solution (5.11) shows that the surface vorticity reverses simultaneously at all points on the sphere. Thus there is no definable angle of separation $\Delta\theta_s$ for Stokes flow. The effect of nonlinear convective acceleration by the flow is to introduce phase variations in the reversal of surface vorticity at different locations on the sphere. Thus for the flow sequence of figures 11 and 12 the point of separation begins at $\theta = \pi$ and
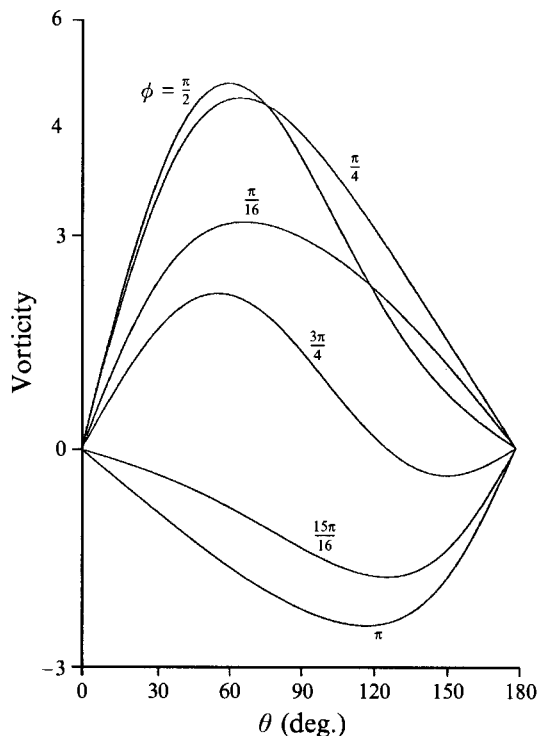
FIGURE 14. Surface vorticity over half an oscillation cycle for $Re = 16.7$ and $S_t = 0.625$ at $\phi = \pi/16, \pi/4, \pi/2, 3\pi/4, 15\pi/16$, and π.

moves to $\theta = 0$ as the phase ϕ increases. At moderate Reynolds numbers and lower values of S_t separation appears soon after the flow starts to decelerate at $\phi = \pi/2$, and ϕ_s increases towards $3\pi/4$ as the oscillation frequency is increased. These trends are discernible in the results of table 2. From these results we may conclude that except for very low Reynolds and Strouhal numbers the reversal of the surface shear stress, and the appearance of a separation region, will exhibit a phase lead over the free-stream velocity.

5.3. Steady streaming

Steady streaming refers to the time-averaged mean flow generated by the Reynolds stress during the cycle. Streaming due to a sphere undergoing low-amplitude oscillations has been studied by Riley (1966) who considered the four low-amplitude cases given as I: $M = O(1)$, II: $Re = O(1)$, III: $Re_s = Re/S_t \geqslant O(1)$, and IV: $M \ll 1$. Re_s is the Reynolds number associated with the streaming outside the surface shear layer and is given as $Re_s = \max|U(t)|^2/\sigma v$. In cases I and II a thin oscillatory Stokes shear layer is formed near the sphere. In the shear layer the nonlinear convective acceleration generates a mean flow and induces a mean flow outside the shear layer. The steady flow outside this layer adjusts to the free-stream conditions in a Stokes flow manner, since S_t is large and Re_s small, with vorticity diffused throughout the flow field. For case III a double boundary layer is formed where the vorticity of the outer streaming flow is also confined within a boundary layer, the shear wave layer is embedded within this boundary layer and both are confined to an area near
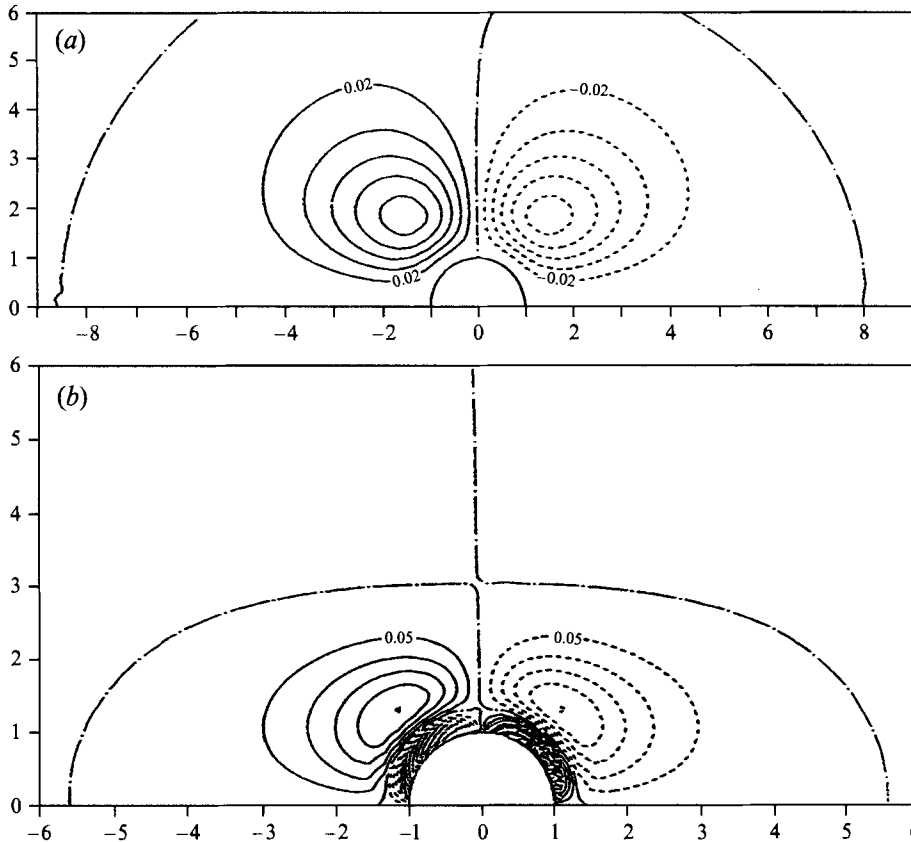
FIGURE 15. Steady streaming patterns for $Re = 16.7$ and $S_t = 0.625$. (a) Time-averaged stream function, $\overline{\psi}$, over an oscillation cycle; $\overline{\psi} < 0$ (— — —), $\overline{\psi} = 0$ (— · —·), and $\overline{\psi} > 0$ (———). (b) Time averaged vorticity, $\overline{\omega}$, over an oscillation cycle; $\overline{\omega} < 0$ (— — —), $\overline{\omega} = 0$ (— · —·), and $\overline{\omega} > 0$ (———).

the sphere. In case IV the shear-wave layer is found to be large with the vorticity extending far into the flow field away from the sphere.

Figure 15(a) shows the time-averaged stream function over an oscillation cycle for $Re = 16.7$ and $S_t = 0.625$. Here the amplitude of the oscillations is somewhat large (1.6 sphere radii) and the flow does not fall under any of the low-amplitude cases considered by Riley. The presence of steady streaming is seen in the form of counter-rotating standing eddy regions that are reflection-symmetric with respect to the sphere equator and flow centreline. These regions appear to be confined to a region near the sphere indicating the existence of a second outer streaming region and a double boundary-layer structure. Figure 15(b) shows the time-averaged vorticity associated with this steady streaming. Two distinct regions of vorticity are seen suggesting such a structure. A double boundary-layer structure is more clearly seen in figure 16 where the Strouhal number has been increased to $S_t = 10$ with the Reynolds number remaining at $Re = 16.7$. This flow falls under classification III where $Re_s \geqslant O(1)$.

An example of a streaming pattern without a double boundary-layer structure is shown in figure 17 where $Re = 0.1$ and $S_t = 0.625$. Since the Reynolds number is very low and the oscillation amplitudes somewhat large, the diffusive lengthscale is much greater than a typical length a indicating that inner and outer streaming regions are
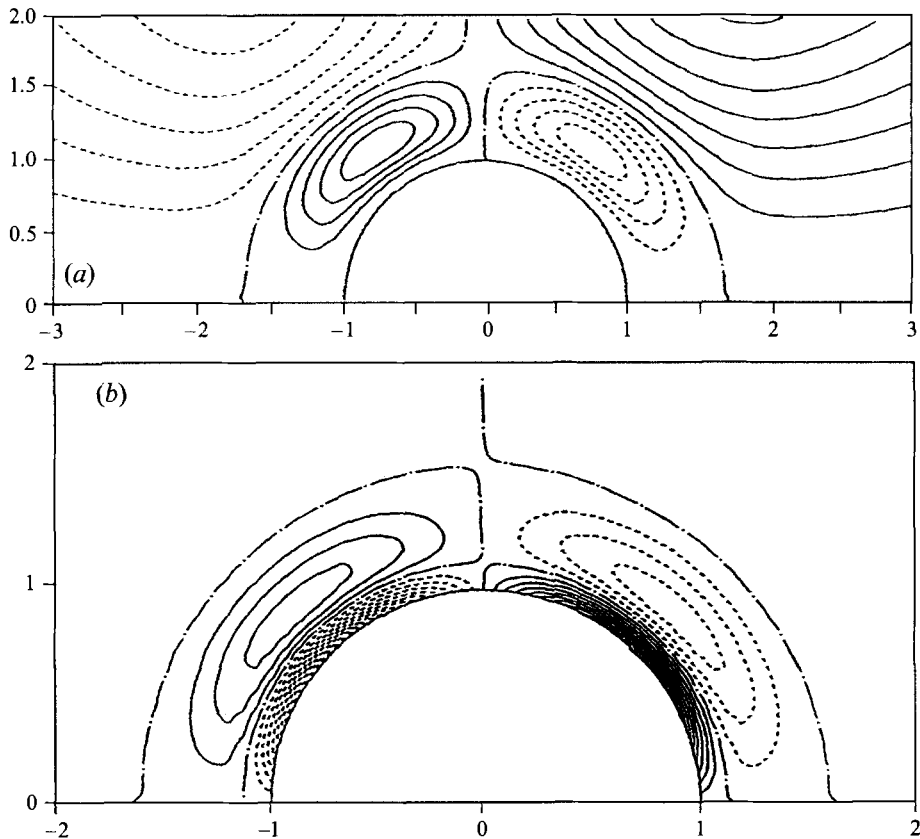
FIGURE 16. Steady streaming patterns for $Re = 16.7$ and $S_t = 10.0$. (a) Time averaged stream function over an oscillation cycle; $\overline{\psi} < 0$ (– – –), $\overline{\psi} = 0$ (– · –·), and $\overline{\psi} > 0$ (——). (b) Time averaged vorticity over an oscillation cycle; $\overline{\omega} < 0$ (– – –), $\overline{\omega} = 0$ (– · –·), and $\overline{\omega} > 0$ (——).

not expected. The recirculation and outer vorticity regions extend throughout the flow field.

Table 3 shows results for several different Reynolds and Strouhal number combinations. Riley found $Re_S \gg 1$ to be a necessary and sufficient condition for a low-amplitude oscillatory flow to have a double-boundary layer structure. Our data suggest that this is not the case for high-amplitude (low-S_t) flows, regardless of the Reynolds number. For the cases included in this investigation, the only ones exhibiting two streaming regions are those where $Re_S \geqslant O(1)$ with low- to moderate-amplitude oscillations. There do not appear to be any generalizations that can be made for the existence of inner and outer streaming regions for flows of all amplitudes.

The generation of steady streaming is associated with the production of higher harmonics of the oscillation frequency through nonlinear inertial effects. A frequency spectrum of the flow indicates the strength of these effects. Figure 18 shows the Fourier time decomposition of the vorticity field at various (r, θ) positions for $Re = 16.7$ and $S_t = 0.625$. These spectra were obtained by sampling every $\phi/32$ over 10 periods. At $(r, \theta) = (1.79, 25\pi/64)$ the mean vorticity, while lower in magnitude than the forcing frequency, is quite significant. Both even and odd harmonics are active and decay with increasing frequency. The second harmonic is more than a decade lower than the forcing frequency and the sixth harmonic is seven decades lower. Much further
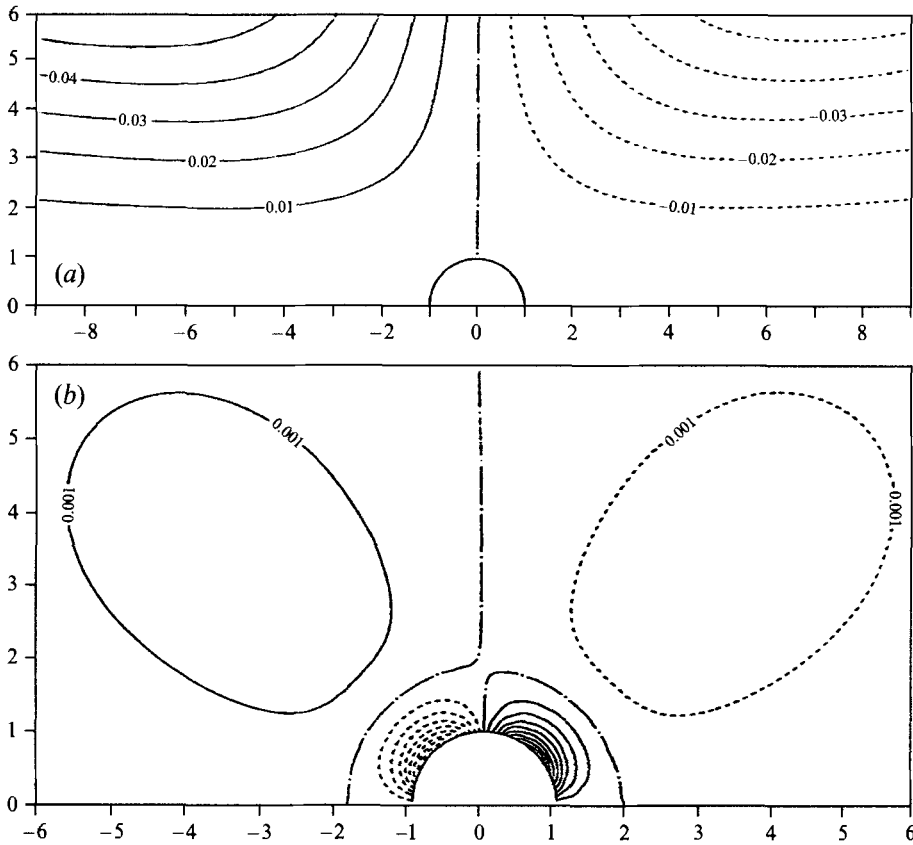
FIGURE 17. Steady streaming patterns for $Re = 0.1$ and $S_t = 0.625$. (a) Time averaged stream function over an oscillation cycle; $\overline{\psi} < 0$ (— — —), $\overline{\psi} = 0$ (— · —), and $\overline{\psi} > 0$ (——). (b) Time averaged vorticity over an oscillation cycle; $\overline{\omega} < 0$ (— — —), $\overline{\omega} = 0$ (— · —), and $\overline{\omega} > 0$ (——).

Re	S_t	Re_S	M^2	δ_S	δ	Cat.	Rec.
16.7	0.625	26.8	5.23	0.44	0.36	-	2
16.7	10.0	1.67	83.7	0.11	0.12	III	2
0.1	0.625	0.16	0.03125	5.65	0.89	-	1
16.7	0.1	167.0	0.837	1.09	0.46	-	1
0.01	10.0	0.001	0.05	4.47	0.86	IV	1
0.1	10.0	0.01	0.5	1.41	0.64	I	1
1.0	10.0	0.1	5.0	0.447	0.36	II	1
10.0	10.0	1.0	50.0	0.141	0.14	III	2
0.1	0.10	1.0	0.005	14.1	0.93	-	1
1.0	0.10	10.0	0.05	4.47	0.86	-	1
10.0	0.10	100.0	0.50	1.41	0.50	-	1

TABLE 3. Stokes shear-wave thickness, $\delta_S = (\nu/\sigma)^{1/2}$; length of mean surface-generated inner vorticity layer, δ; categorization, Cat. (see text); and number of recirculation regions, Rec.; for various Re and S_t combinations. Here $Re_S = Re/S_t$ and $M^2 = \frac{1}{2} Re S_t$

from the surface, at $(r, \theta) = (19.5, 7\pi/32)$, the vorticity is much weaker. Here, there are only three active modes, including the mean, and they are all lower in magnitude than the sixth harmonic at the first location. At position $(r, \theta) = (1.06, \pi/2)$, which is on the axis of symmetry, there is no mean vorticity present. The vorticity here is composed strictly of rapidly decaying odd harmonics; the fifth harmonic is seven decades below the fundamental. Fourier spectra for the velocity components behave similarly and are not shown.

5.4. *Forces*

The viscous drag force and pressure force on the sphere for $Re = 16.7$ and $S_t = 0.625$ over one oscillation cycle are shown in figure 19. A phase lead is evident in the frictional component; the viscous force changes sign before the free-stream velocity. This is due to the recirculation region formed following flow separation during the decelerating period of the oscillation cycle. The strength and size of this region at a certain point becomes the dominant flow feature near the sphere. When the amount of negative surface vorticity is greater than the amount of positive vorticity, the viscous drag force (2.19) will be negative. Table 4 gives the phase angles, ϕ_f, ϕ_p, and ϕ_d, at which the viscous, pressure and total drag coefficients, respectively, change sign. At low S_t, $\phi_f \rightarrow \pi$, indicating that for high-amplitude oscillations the frictional force is nearly in phase with the forcing velocity. For increasing S_t or decreasing Re the anticipated value $\phi_f \rightarrow 3\pi/4$ is approached as convective effects diminish. The pressure drag force also exhibits a phase lead over the free-stream velocity. At high values of S_t acceleration effects dominate the composition of the pressure drag force. For a free stream oscillating with $U(t) = -\sin \phi$ the added-mass force in both the Stokes flow and inviscid flow cases is proportional to $S_t \cos \phi$. For high S_t, this will dominate the pressure component of the drag yielding the computed result that $\phi_p \rightarrow \pi/2$. The combined result is that there exists a phase lead for all but the lowest S_t–Re combinations; the force on the sphere changes sign before the flow reverses direction. This is significant because it indicates that under the correct conditions, instead of retarding the fluid flow, the presence of the sphere can act to maintain the flow.

The Fourier time decomposition of C_d for $Re = 16.7$ and $S_t = 0.625$ is shown in figure 20. The small mean component seen is a residual due to the initial start up and is small enough to be ignored. The force spectrum is composed of the fundamental forcing frequency of the free-stream velocity and, owing to the axial symmetry of the flow, odd harmonics of this frequency. The spectra decay quite rapidly with the fifth harmonic being seven magnitudes below the fundamental. The spectra for the individual components exhibit almost identical behaviour, with only a few modes containing any real energy.

Based on their experimental data for the forces on an oscillating sphere, Odar & Hamilton (1964) proposed an empirical relationship between the force and the velocity and acceleration conditions for use at low to moderate Reynolds numbers. The relationship is an extension of the Basset formula and contains estimated contributions from a quasi-steady drag force at the same corresponding instantaneous Reynolds number, an added-mass term and a history term. The form of the history integral was assumed to be the same as in unsteady Stokes flow (5.9) but with an empirically determined coefficient Q_H multiplying the final result. Corresponding to (5.10) their estimate for the force on a sphere placed in an oscillating free stream is

$$- C_{dOH} = (1 + Q_A)\tfrac{4}{3}S_t \cos \phi + \tfrac{1}{2}Q_D| \sin \phi| \sin \phi + 2Q_H(M/Re) \cos(\phi - \pi/4), \quad (5.13)$$
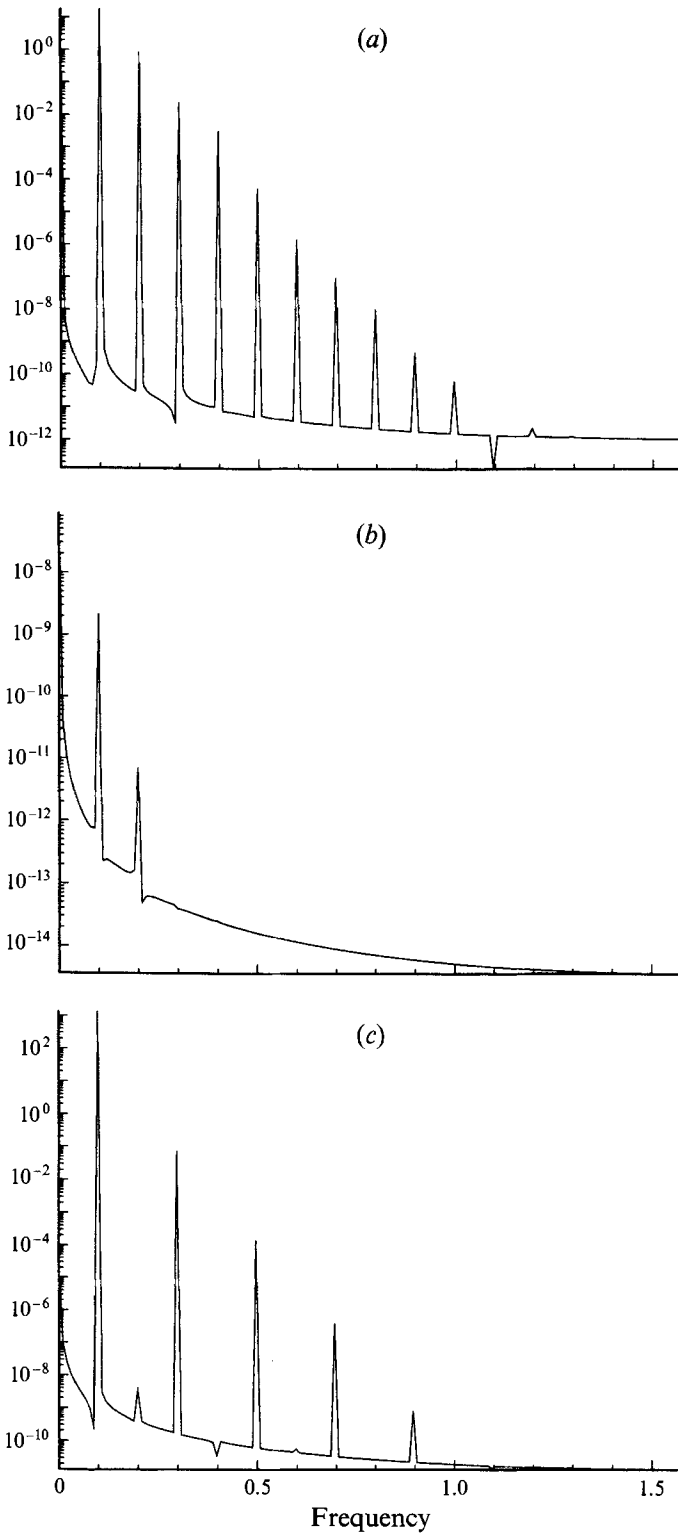
FIGURE 18. Fourier time spectrum of the vorticity at different (r, θ) locations: (a) $(1.79, 25\pi/64)$, (b) $(19.5, 7\pi/32)$, and (c) $(1.06, \pi/2)$. The data were sampled every $\phi/32$ for ten oscillation cycles.
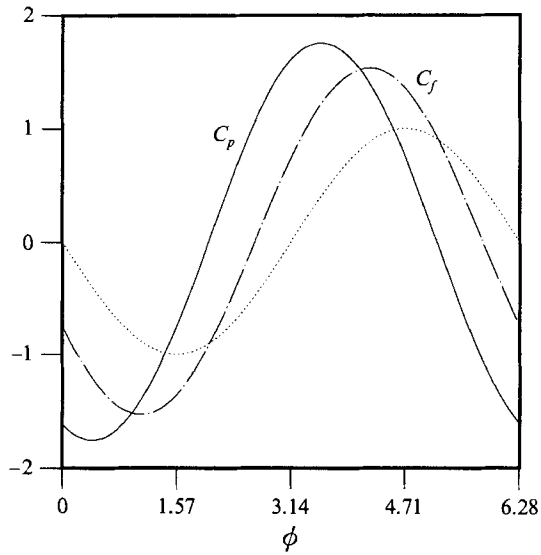
FIGURE 19. Frictional and pressure drag forces, C_f and C_p for $Re = 16.7$ and $S_t = 0.625$. The free-stream velocity is shown by the dotted line, ϕ is the phase angle of the oscillation in radians.
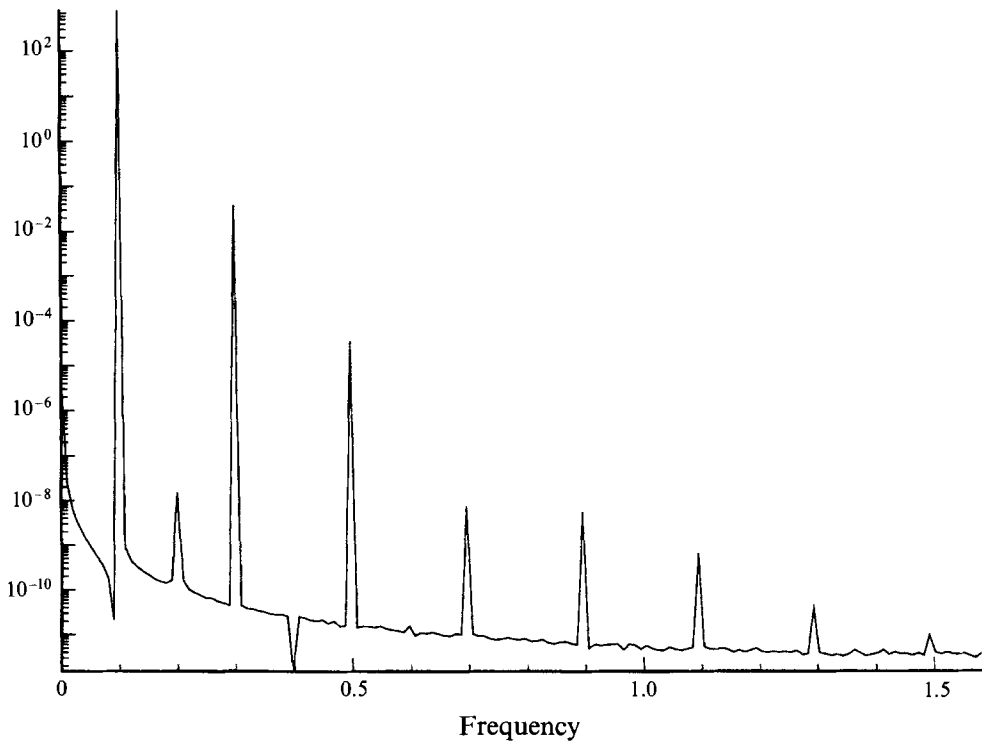

FIGURE 20. Fourier time spectrum of C_d for $Re = 16.7$ and $S_t = 0.625$.

Re	S_t	ϕ_f	ϕ_p	ϕ_d
0.1	0.625	3.03	3.00	3.02
1.0	0.625	2.87	2.67	2.80
5.0	0.625	2.73	2.26	2.53
10.0	0.625	2.67	2.10	2.40
16.7	0.1	2.88	2.51	2.74
16.7	1.0	2.58	1.89	2.17
16.7	2.5	2.50	1.75	1.97
16.7	0.625	2.64	2.01	2.30
16.7	10.0	2.43	1.65	1.79
0.1	10.0	2.82	2.55	2.72
1.0	10.0	2.59	1.94	2.24
10.0	10.0	2.45	1.68	1.84
0.1	0.1	3.10	3.09	3.10
1.0	0.1	3.02	2.97	3.00
10.0	0.1	2.91	2.64	2.80

TABLE 4. Phase angle at which frictional, pressure, and total drag coefficients ϕ_f, ϕ_p, and ϕ_d change sign

where ϕ is again the phase angle $S_t t$. The coefficients are specified as functions of the instantaneous Reynolds number $Re(t) = Re|\sin\phi|$ and the instantaneous acceleration number $Ac(t) = Ac\sin^2\phi/|\cos\phi|$, taking absolute values. Odar (1966) gives the coefficients as

$$Q_A = 1.05 - 0.066/(Ac(t)^2 + 0.12), \quad Q_H = 2.88 + 3.12/(Ac(t) + 1)^3, \quad (5.14)$$

which interpolates the estimated values from the experiments. The equivalent steady flow drag coefficient Q_D is determined by $Re(t)$, and Odar & Hamilton used the empirical results of Lapple (1951) to evaluate Q_D and separate it from the other terms. In figure 21 we have evaluated (5.13) for $Re = 16.7$ and $S_t = 0.625$, reconstructing the procedure of Odar & Hamilton. This model result may be compared with the present numerical simulations and the actual measured values shown in figure 10. It is also of interest to compare these results with the simple Basset rule (5.10) which is also shown. The Odar model is no more accurate in this example than the Basset result, though the Basset solution obviously has none of the higher harmonics evident in figure 20.

According to the Basset solution (5.10) and Odar & Hamilton's model (5.13) the effect of the history term is zero at a phase angle $\phi = 3\pi/4$. The latter used this assumption to infer separately the contributions to C_d from added-mass effects and the history term. In both inviscid potential flow and unsteady Stokes flow the added-mass term appears as inviscid contribution to the pressure force C_p with a coefficient Q_A equal to 0.5. For general viscous flow with vorticity, the main issue is to define clearly what is meant by an added-mass effect since viscous processes will modify both the kinetic energy and momentum changes in an unsteady flow. This issue is taken up in a companion paper (Part 2) and for oscillatory flows it is not a simple matter to separate out unambiguously the various contributions. The assumption of Odar & Hamilton regarding the vanishing of the history term at $\phi = 3\pi/4$ is probably incorrect, since it is linked to the assumption that the integral varies linearly with the square root of the oscillation frequency. Mei *et al.* (1991) and Mei & Adrian (1992) have demonstrated that for unidirectional, oscillatory motion at low frequencies or
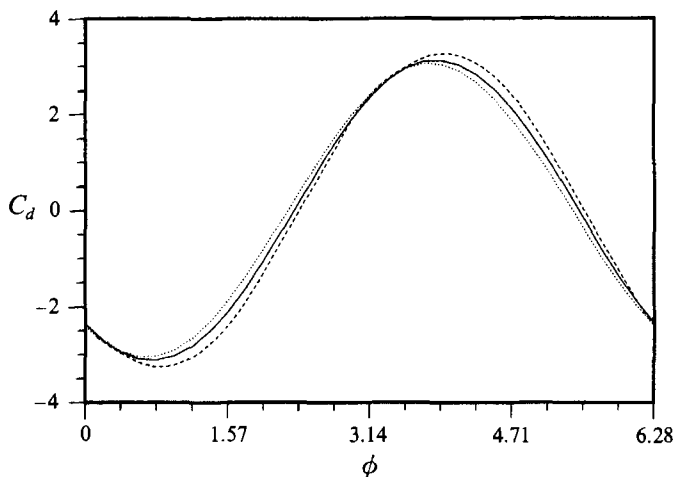
FIGURE 21. Simulation results (solid curve) for C_d at $Re = 16.7$ and $S_t = 0.625$ over an oscillation cycle compared to the Odar & Hamilton model C_{dOH} (- - -), and Basset result C_{dB} ($\cdots$).
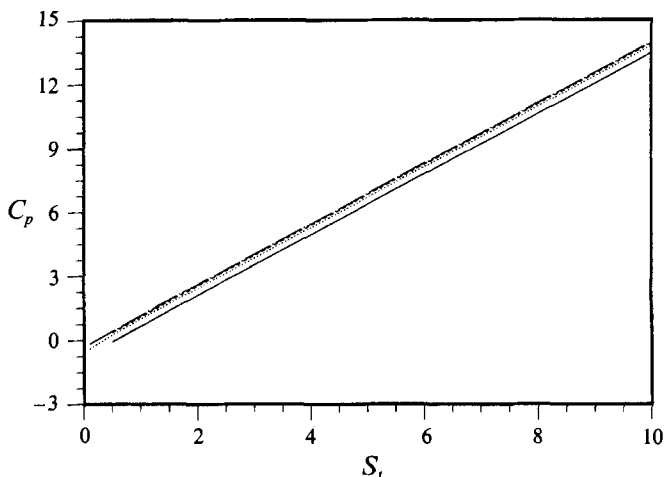

FIGURE 22. C_p as a function of S_t at $\phi = 3\pi/4$. $Re = 4.18$ (——), $Re = 8.27$ ($\cdots$), $Re = 12.6$ (- - -), $Re = 16.7$ (- $\cdot$ -).

for the long term in accelerated motion, advection of vorticity rather than viscous diffusion is more significant and this gives a more rapid decay of the history kernel.

Nevertheless it is of interest to examine the value of the pressure for C_p at the phase angle $\phi = 3\pi/4$ to see how it varies with non-dimensional frequency S_t and Reynolds number Re. The results from the simulations are shown in figure 22. The classical result, $Q_A = 0.5$, would imply an inertial contribution

$$C_P^I(\phi) = -2S_t \cos \theta \qquad (5.15)$$

to the pressure force, which at $\phi = 3\pi/4$ would give C_p^I equal to $\sqrt{2}S_t$. Over the range $0.5 < S_t < 10$ the slopes of the curves are approximately constant with values varying between 1.42 and 1.43. There is a small offset in the value of C_p since there will still be a viscous contribution even if the history term were instantaneously zero.

These results are consistent with (5.15) and lend support to the view that Q_A is 0.5 irrespective of Reynolds number and acceleration number.

Rivero (1991) and Rivero *et al.* (1991) have reported numerical simulations, based on a finite volume-element method, for unsteady axisymmetric flow past a sphere. They present results for simple oscillatory flow (5.6) at a peak Reynolds number $Re = 100$ and for frequencies S_t equal to π and 0.1π. Their results for the force on the sphere and the surface vorticity distribution are consistent with those presented here. They decomposed the force C_d into a quasi-steady drag force involving Q_D, an added-mass term and a history term. The value of Q_D was found directly from simulations in steady flows at the same instantaneous Reynolds number. The added-mass effect was defined as the inertial contribution to C_p dependent on the instantaneous acceleration. This was evaluated at specific phase angles ϕ_0 by computing the flow up to $\phi = \phi_0$ and then performing two separate short computations, one where the free-stream flow continued to accelerate and the other where the flow ceased to accelerate but continued at the same Reynolds number. By taking a short enough interval $\Delta\phi$ they determined the acceleration contribution to C_p and found the corresponding value of Q_A to be 0.5 at each phase angle tested. The remaining history force did not vanish at $\phi = 3\pi/4$, but at a slightly earlier phase angle.

We have not pursued this type of force decomposition with the present simulation results. The flow structure in oscillatory motion is clearly quite different in general from the equivalent steady flow conditions at the same Reynolds number, and it is somewhat arbitrary to decompose the force into a quasi-steady component and a history term as has been adopted in the past. It is also surprising that some of the empirical models may not present a major advantage over the Basset solution (5.10) as a first approximation to the total force.

6. Conclusions

Our investigation of oscillating flow past a sphere has yielded several interesting results. In a steady flow, we found that flow separation did not occur for $Re \leqslant 20$. However, we have found that separation is possible at these Reynolds numbers for an oscillating flow. The existence of a separation region is important because it acts to diminish the viscous forces on the sphere; in many cases the recirculation is large enough to generate a negative force. Besides lowering the viscous force, the separation bubble creates an asymmetry in the flow; the accelerating and decelerating phases of the oscillation cycle are not direct opposites of each other and create time-independent streaming patterns.

The two parameters, S_t and Re, play important roles in determining the exact nature of the separation region. We found that for a given phase angle the length of the separation region decreases but encompasses more of the sphere for increasing S_t (decreasing amplitude). As the Strouhal number is increased, the surface vorticity becomes more symmetric about the sphere equator and increases in intensity. However, this vorticity remains within the Stokes shear layer and does not fully diffuse into the flow field. The role of the Reynolds number is similar in nature. At very low Reynolds and Strouhal numbers, the shear stress is found to remain in phase with the forcing velocity. When a recirculation region is present, increasing the Reynolds number acts to lengthen the region, but reduce its breadth. Decreasing the Reynolds number not only changes the shape of the region, but also delays separation.

Steady streaming patterns generated by finite-amplitude oscillations were quali-tatively similar to those predicted by Riley (1966) for small-amplitude oscillations.

Double boundary-layer structures were found only for flows where $Re_s \geqslant O(1)$. While $Re_s \geqslant O(1)$ is a necessary and sufficient condition for a double boundary layer to exist in a low-amplitude flow, it is found to not be sufficient at higher amplitudes. Our results are consistent with the preliminary observations reported by Drummond & Lyman (1990), although the grid resolution of 15×21 points for their computations was much coarser than that used here. At $Re = 20$ and $S_t = 0.5$ they observed steady streaming with a streamline pattern similar to figure 15, although without a double boundary-layer structure.

Not only can the viscous force on the sphere exhibit a phase lead over the forcing velocity, but the pressure force was shown to exhibit a phase lead as well. This is due to the acceleration effects which increase with importance as the Strouhal number increases. In a companion paper we explore the flow characteristics and forces on a sphere in flows with constant acceleration or deceleration. For these it is possible to unambiguously determine the added mass coefficient and we find it to be indeed 0.5, in agreement with the findings of Rivero et al. (1991).

REFERENCES

Auton, T. R., Hunt, J. C. R. & Prudhomme, M. 1988 The force exerted on a body in inviscid steady non-uniform rotational flow, *J. Fluid Mech.* **197**, 241–257.

Bassett, A. B. 1888 *A Treatise in Hydrodynamics*, Vol. II. Deighton, Bell, and Co.

Batchelor, G .K. 1967 *An Introduction to Fluid Dynamics* Cambridge University Press.

Bentwich, M. & Miloh, T. 1978 The unsteady matched Stokes-Oseen solution for the flow past a sphere. *J. Fluid Mech.* **88**, 17–32.

Brabston, D. C. & Keller, H. B. 1975 Viscous flows past spherical gas Bubbles, *J. Fluid Mech.* **69**, part 1, 179–189.

Chang, E. 1992 Accelerated motion of rigid spheres in unsteady flow at low to moderate Reynolds numbers, PhD thesis, Brown University.

Chang, E. J. & Maxey, M. R. 1994 Unsteady flow about a sphere at low to moderate Reynolds number. Part 2. Accelerated motion. *J. Fluid Mech.* (submitted).

Chester, W. & Breach, D. R. 1969 On the flow past a sphere at low Reynolds number. *J. Fluid Mech.* **37**, 751–760.

Clift, R., Grace, J. R. & Weber, M. E. 1978 *Bubbles, Drops, and Particles*. Academic.

Dennis, S. C. R. & Walker, J. D. A. 1971 Calculation of the steady flow past a sphere at low and moderate Reynolds numbers. *J. Fluid Mech.* **48**, 771–789.

Dennis, S. C. R. & Walker, J. D. A. 1972 Numerical solutions for time-dependent flow past an impulsively started sphere. *Phys. Fluids* **15**, 517–525.

Drummond, C. K. & Lyman, F. A. 1990 Mass transfer from a sphere in an oscillating flow with zero mean velocity. *Comput. Mech.* **6**, 315–326.

Fornberg, B. 1988 Steady viscous flow past a sphere at high Reynolds numbers. *J. Fluid Mech.* **190**, 471–489.

Goldstein, S. 1929 The forces on a solid body moving through viscous fluid. *Proc. R. Soc. Lond.* A **123**, 216–235.

Homann, F. 1936 The effect of high viscosity on the flow around a cylinder and around a sphere. *NACA. Tech Mem.* 1334.

Keulegan, G. H. & Carpenter, L. H. 1958 Forces on cylinders and plates in an oscillating fluid. *J. Res. Nat. Bur. Stand.* **60**, 423–440.

Kim, J., Moin, P. & Moser, R. 1987 Turbulence statistics in fully developed channel flow at low Reynolds number. *J. Fluid Mech.* **177**, 133–166.

Kim, I. & Pearlstein, A. J. 1990 Stability of flow past a sphere. *J. Fluid Mech.* **211**, 73–93.

Lane, C. A. 1955 Acoustical streaming in the vicinity of a sphere. *J. Acoust. Soc. Am.* **27**, 1082–1086.

Lapple, C. E. 1951 Particle dynamics. Eng. Res. Lab., Eng. Dept., E.I. du Pont de Nemours and Co., Inc., Wilmington, Delaware.

Le Clair, B. P., Hamielec, A. E., & Pruppracher, H. R. 1970 A numerical study of the drag on a sphere at low and intermediate Reynolds numbers, *J. Atmos. Sci.* **27**, 308–315.

Lin, C. L. & Lee, S. C. 1973 Transient state analysis of separated flow around a sphere, *Compu. Fluids* **1**, 235–250.

Marcus, P. S. & Tuckerman, L. S. 1987 Simulation of flow between concentric rotating spheres. Part 1. Steady states *J. Fluid Mech.* **185**, 1–30.

Maxey, M. R. & Riley, J. J. 1983 Equation of motion for a small rigid sphere in a nonuniform flow. *Phys. Fluids* **26**, 863–889.

Mei, R. & Adrian, R. J. 1992 Flow past a sphere with an oscillation in the free-stream velocity and unsteady drag at finite Reynolds number. *J. Fluid Mech.* **237**, 323–341.

Mei, R., Lawrence, C. J. & Adrian, R. J. 1991 Drag on a sphere with fluctuations in the free stream velocity. *J. Fluid Mech.* **233**, 613–631.

Natarajan, R. & Acrivos, A. 1993 The instability of the steady flow past spheres and disks. *J. Fluid Mech.* **254**, 323–344.

Odar, F. 1964 Forces on a sphere accelerating in a viscous fluid. *US Army Cold Regions Research and Engineering Laboratory, Research Rep.* 128.

Odar, F. 1966 Verification of the proposed equation for calculation of the forces on a sphere accelerating in a viscous fluid. *J. Fluid Mech.* **25**, 591–592.

Odar, F. & Hamilton, W. S. 1963 Forces on a sphere accelerating in a viscous fluid. *J. Fluid Mech.* **18**, 302–314.

Oliver, D. L. R. & Chung, J. N. 1985 Flow about a fluid sphere at low to moderate Reynolds numbers. *J. Fluid Mech.* **177**, 1–18.

Orszag, S. A. 1974 Fourier series on spheres. *Mon. Weath. Rev.* **102**, 56–75.

Proudman, I. & Pearson, J. R. A. 1957 Expansions at small Reynolds numbers for the flow past a sphere and a circular cylinder. *J. Fluid Mech.* **2**, 237–262.

Riley, N. 1966 On a sphere oscillating in a viscous fluid. *Q. J. Mech. Appl. Maths* **19**, 461–472.

Rimon, Y. & Cheng, S. I. 1969 Numerical solution of a uniform flow over a sphere at intermediate Reynolds number. *Phys. Fluids* **12**, 949–959.

Rivero, M. 1991 Etude par simulation numerérique des forces exercées sur une inclusion sphérique par un écoulement accéléré, Thèse de Doctorat, I.N.P.T.

Rivero, M., Magnaudet, J. & Fabre, J. 1991 Quelques Résultants nouveaux concernant les forces exercées sur une inclusion sphérique par en écoulement accéléré, *C.R. Acad. Sci. Paris*, **312**, (I), 1499–1506.

Sano, T. 1981 Unsteady flow past a sphere at low Reynolds number. *J. Fluid Mech.* **112**, 433–441.

Taneda, S. 1956 Experimental investigation of the wake behind a sphere at low Reynolds numbers. *J. Phys. Soc. Japan* **11**, 302.

Tomboulides, A. G., Orszag, S. A., & Karniadakis, G. E. 1993 Direct and large-eddy simulation of axisymmetric wakes. *AIAA Paper* 93-0546.